

ROBUST FRACTAL CHARACTERIZATION OF ONE-DIMENSIONAL  
AND TWO-DIMENSIONAL SIGNALS

by

NIRANJAN AVADHANAM, B.Tech.

A THESIS

IN

ELECTRICAL ENGINEERING

Submitted to the Graduate Faculty  
of Texas Tech University in  
Partial Fulfillment of  
the Requirements for  
the Degree of

MASTER OF SCIENCE

IN

ELECTRICAL ENGINEERING

Approved

---

Chairperson of the Committee

Accepted

---

Dean of the Graduate School

AC  
805  
.A93  
1993

August, 1993

## ACKNOWLEDGMENTS

I would like to express my sincere gratitude to my thesis advisor, Dr. Sunanda Mitra for her encouragement and guidance. I would also like to extend my appreciation to Dr. William J.B. Oldham and Dr. Thomas F. Krile for their guidance and for serving on the graduate committee.

I also appreciate the support and encouragement offered by my friends. Finally, I would like to thank my parents for their love and encouragement and my sister for believing in me.

## TABLE OF CONTENTS

ACKNOWLEDGMENTS	ii
ABSTRACT	v
LIST OF TABLES	vi
LIST OF FIGURES	vii
CHAPTER	
1. INTRODUCTION	1
1.1 Outline of the Thesis	2
2. FRACTAL GEOMETRY	3
2.1 Introduction	3
2.2 Fundamental Concepts and Definitions	3
2.2.1 Fractal Dimension : Definition	9
3. FRACTIONAL BROWNIAN MOTION	11
4. GENERATIVE METHODS	14
4.1 Midpoint Displacement method	14
4.2 Spectral Synthesis	15
4.3 Weierstrass Sine Function	15
4.4 Cholesky Decomposition	16
5. ESTIMATION METHODS	20
5.1 Introduction	20
5.2 Power Spectral Density of Fractional Gaussian Noise	20
5.3 Relative Dispersion	21
5.4 Maximum Likelihood Estimation	22

5.4.1 Introduction	22
5.4.2 Maximum Likelihood Estimation	22
5.4.3 Application of MLE to DFGN	23
5.4.4 MLE for noisy data	24
5.4.4.1 Lilliefors Test	25
5.4.4.2 Cramer-Von Mises Test	25
5.4.5 MLE for the Gaussian Noise Model	26
6. RESULTS FOR ONE-DIMENSIONAL DATA	27
7. TEXTURE ANALYSIS	31
7.1 Introduction	31
7.2 Fractal Characterization of Textures	32
7.2.1 Texture Classification	33
7.2.2 Texture Segmentation	36
8. CONCLUSIONS AND FUTURE WORK	46
REFERENCES	47
APPENDIX	
A. CRAMER-VON MISES TEST PERCENTAGE POINTS	51
B. LILLIEFORS TEST SIGNIFICANCE VALUES	52

## ABSTRACT

Fractals have been shown to be useful in the analysis of time series data and in classification of natural shapes and textures. A Maximum Likelihood Estimator is used to measure the parameter  $H$  which is directly related to the fractal dimension. The robustness of the estimator is shown in the presence of noise. The performance of the method is demonstrated on datasets generated using a variety of techniques. Finally the performance of the estimator is shown by characterization of homogenous textures and by the segmentation of noisy composite images of natural textures.

## LIST OF TABLES

6.1 Results of estimation on data sets generated using Midpoint Displacement	29
6.2 Results of estimation on data sets generated using Weierstrass method	29
6.3 Results of estimation on data sets generated by Spectral Synthesis	30
6.4 Results of estimation on data sets generated by Cholesky Decomposition	30
6.5 Results of estimation on noisy Data Sets generated by Cholesky Decomposition S/N 30 db	30
A.1 Lower tail percentage points for $w_N^2$ for the Cramer-Von Mises test	51
A.2 Upper tail percentage points for $w_N^2$ for the Cramer-Von Mises test	51
B.1 Level of Significance for D for Lilliefors test	52

## LIST OF FIGURES

2.1 Construction of Van Koch Curve : Iterations 1-6	5
2.2 Construction of the Peano space-filling Curve : Iterations 1-4	8
4.1 FBM Samples for $H=0.9$ , $H=0.4$ and $H=0.1$	17
4.2 FGN Samples for $H=0.9$ , $H=0.4$ and $H=0.1$	17
4.3 FBM Samples for $H=0.9$ , $H=0.4$ and $H=0.1$ with S/N 30db	18
4.4 FGN Samples for $H=0.9$ , $H=0.4$ and $H=0.1$ with S/N 30db	18
4.5 Fractal Brownian surfaces for $H=0.9$ , $H=0.4$ and $H=0.1$	19
7.1 Histogram of pixel differences for a typical textured path	34
7.2 Single homogenous texture polymer image	35
7.3 Histogram of fractal dimensions for the homogenous texture image	35
7.4 Homogenous Brodatz texture (Burlap)	37
7.5 Histogram of fractal dimensions for Burlap	37
7.6 Composite texture polymer image	38
7.7 Histogram of fractal dimensions for the composite texture Image	38
7.8 Result of segmentation of composite polymer image	41
7.9 Composite Brodatz texture image	42
7.10 3-D plot of the fractal dimensions for the composite image	42
7.11 Histogram of fractal dimensions for the composite Brodatz texture	43
7.12 Results of segmentation of the Brodatz image	43
7.13 Histogram of fractal dimensions for the noisy Brodatz texture	44
7.14 Result of segmentation of the noisy Brodatz composite image	44
7.15 Result of segmentation of composite image shown as a 3-D plot	45
7.16 Result of segmentation of noisy image shown as a 3-D plot	45

## CHAPTER 1

### INTRODUCTION

Fractals are mathematical sets with a high degree of geometrical complexity that can model many natural phenomena such as mountains, coastlines as well as images obtained from fractal surfaces [1, 3, 4, 19]. Fractal characterization of signals has been shown to be useful in the analysis of time series data and in classification of natural shapes and textures [1, 14, 15, 16, 17, 18]. In particular they have been found to be useful in describing disordered textures [49]. Fractals have been used for speech segmentation and interpolation [10], sound classification [10], and to describe chaos in the capital market [12] and in the electrophysiology of the heart [7]. Fractal modeling has been used to generate [13, 52], interpolate [13], and code [8] images. It has also been used to describe the roughness of surfaces [5] and to describe the surface area of chemical reactants [6]. Fractal probability functions have been applied to Image Analysis [9]. Keller et al. [22] show that global characteristics of natural scenes can be generated using fractals and demonstrate the method on tree and mountain scenes.

In this thesis the application of fractal geometry to the analysis of 1-D and 2-D signals is examined. Discrete Fractional Brownian Motion (DFBM) is considered to characterize the signals. The robustness of the performance of the Power Spectral Density (PSD) method, the Relative Dispersion (RD) method and the Maximum Likelihood Estimation method (MLE) is evaluated on datasets generated using Spectral Synthesis, Midpoint Displacement, Weierstrass-Mandelbrot formula and Cholesky Decomposition.

Images of synthetic polymer membranes and images from the Brodatz album [58] have been used for characterization as fractal brownian surfaces. Finally, the

estimation algorithm is applied to the segmentation of composite texture polymer image and composite Brodatz texture image with and without the presence of noise.

### 1.1. Outline of the Thesis

The thesis is organized as follows : Chapter 2 contains a brief introduction to fractal geometry. Chapter 3 deals with the description of DFBM and Discrete Fractional Gaussian Noise (DFGN). Chapter 4 describes the various generative algorithms used to generate the datasets and Chapter 5 gives the description of the considered estimators. Chapter 6 shows the results of the simulations on 1-D data sets. The performance of the estimators in the presence of additive Gaussian noise is shown. Chapter 7 describes Texture Analysis and the modeling of fractal brownian surfaces. The ML estimator is used for characterization of single textures and for segmentation of noisy composite texture images and the results are explained. Finally, chapter 8 summarizes all the results and conclusions.

## CHAPTER 2

### FRACTAL GEOMETRY

#### 2.1. Introduction

Fractal geometry is a concept introduced by B.B Mandelbrot which provides both a description and a mathematical model for many complex forms in nature which cannot be explained using traditional Euclidean geometry [1]. Euclidean geometry provides concise and accurate descriptions of man made objects but is inappropriate for natural shapes. It yields cumbersome and inaccurate descriptions. Complex shapes such as coastlines, mountains and clouds possess a striking simplifying invariance under changes of magnification. This self-similarity is quantified by the fractal dimension which need not be an integer and which is related to the innate "roughness" of the shape. Fractal shapes are said to be self-similar and independent of scale or scaling [1, 18].

Fractals have blossomed tremendously in the past few years and have connected pure mathematics research with natural sciences and computing. Within the last 5-10 years, fractal concepts have been introduced in most of the natural sciences : physics, chemistry, biology, meteorology and materials science. It has also found application in recent times in diverse engineering disciplines like fracture analysis [54] , analysis of viscous fingering [19] , computer graphics [52], analysis of the cache hit ratio [55] in addition to several applications in electrical engineering.

#### 2.2. Fundamental Concepts and Definitions

The definition of a fractal is given by Mandelbrot [1] as a set for which the Hausdorff- Besicovitch dimension strictly exceeds the topological dimension. In general

the Euclidean and the topological dimensions are the upper and lower limits of the fractal dimension.

$$d_T \leq d_F \leq d_E \quad (2.1)$$

The fractal model is used to relate a metric property such as length of a line or area of a surface to the elemental length or area, i.e., the ruler used as a basis for the calculation.

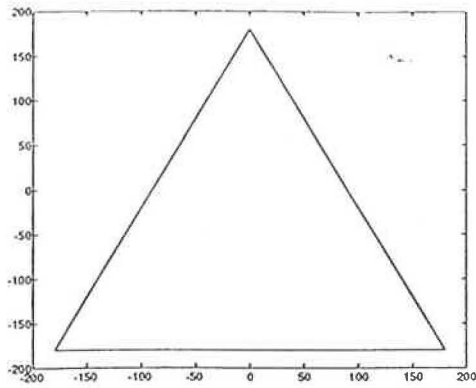
The relationship between the ruler size and length is

$$L(\epsilon) \cong F(\epsilon)^{1-D} \text{ as } \epsilon \rightarrow 0 \quad (2.2)$$

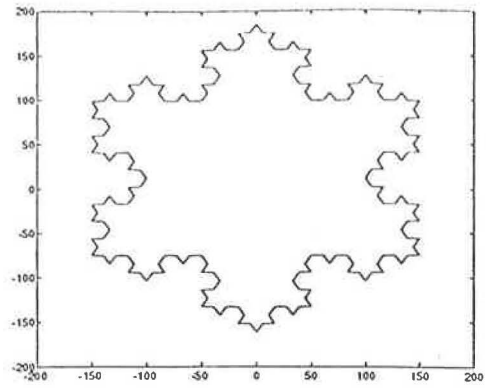
where  $L$  is the total length,  $F$  is the scaling constant,  $\epsilon$  is the elemental ruler length,  $D$  is the fractal dimension.

The construction of the Van Koch snow flake curve is illustrative. Figure 2.1 shows an iterative or recursive procedure for constructing a fractal curve. A simple line segment is divided into thirds and the middle segment is replaced by two equal segments forming part of an equilateral triangle. At the next stage in the construction, each of these four segments is replaced by four new segments with length 1/3 of their parent according to the original pattern. This procedure, repeated over and over, yields the Van Koch curve shown in the figure and demonstrates that the iteration of a very simple rule can produce complex shapes with highly unusual properties. At each stage in its construction the length of the curve increases by a factor of 4/3. Thus, the limiting curve crams an infinite length into a finite area of the plane without intersecting itself. The curve has detail on all length scales. The closer one looks, the more detail one finds. More important, the curve possesses an exact self-similarity. Each small portion, when magnified, can reproduce exactly a larger portion. The curve is said to be invariant under changes of scale.

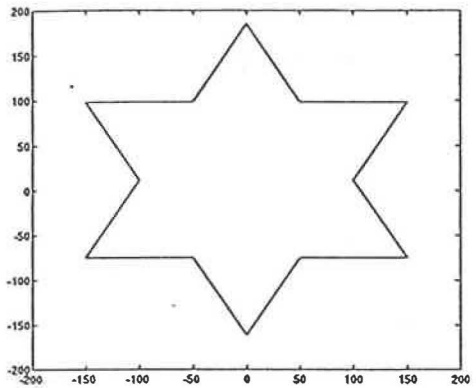
An object normally considered as one-dimensional, a line segment, for example also possesses a similar scaling property. It can be divided into  $N$  identical parts each



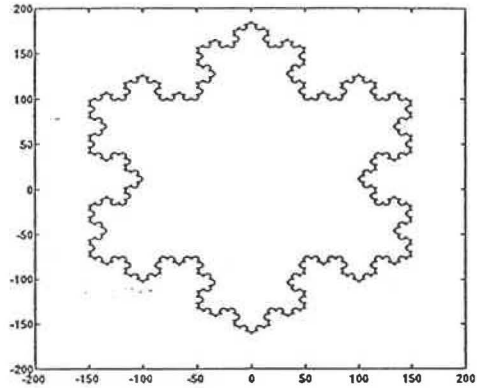
Iteration 0



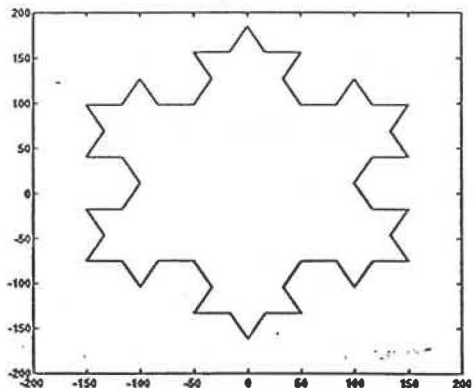
Iteration 4



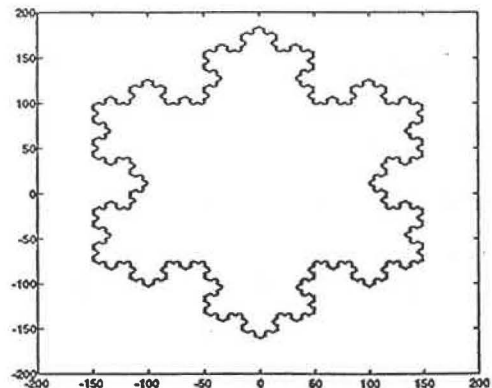
Iteration 1



Iteration 5



Iteration 2



Iteration 6

Figure 2.1 Van Koch Curves

of which is scaled down by the ratio  $r = \frac{1}{N}$  from the whole. Similarly, a two-dimensional object, such as a square area in the plane, can be divided into  $N$  self-similar parts each of which is scaled down by a factor  $r = \frac{1}{\sqrt{N}}$ . A three-dimensional object like a solid cube may be divided into  $N$  little cubes each of which is scaled down by a ratio  $r = \frac{1}{\sqrt[3]{N}}$ . With self-similarity the generalization to fractal dimension is straightforward. A  $D$ -dimensional self-similar object can be divided into  $N$  smaller copies of itself each of which is scaled down by a factor  $r$  where  $r = \frac{1}{\sqrt[D]{N}}$  or

$$N = \frac{1}{r^D} . \quad (2.3)$$

Conversely, given a self-similar object of  $N$  parts scaled by a ratio  $r$  from the whole, its fractal or similarity dimension is given by

$$D = \frac{\log(N)}{\log\left(\frac{1}{r}\right)} . \quad (2.4)$$

The fractal dimension, unlike the more familiar notion of Euclidean dimension, need not be an integer. Any segment of the Von Koch curve is composed of 4 sub-segments each of which is scaled down by a factor of  $1/3$  from its parent. Its fractal dimension is  $D = \frac{\log(4)}{\log(3)}$  or about 1.26. This non-integer dimension, greater than one but less than two, reflects the unusual properties of the curve. It somehow fills more of space than a simple line ( $D=1$ ), but less than a Euclidean area of the plane ( $D=2$ ). As  $D$  increases from 1 towards 2 the resulting curves progress from being line-like to filling

2.2. The fractal dimension thus provides a quantitative measure of the wiggleness of the curves. Although the curves have fractal dimensions between 1 and 2, they all remain a curve with a topological dimension of one. The removal of a single point cuts the curve in two pieces.

The concept of fractal dimension can be applied to statistically self-similar objects which upon magnification look like, but not exactly alike, segments at different scales. When using a ruler of size  $r$  to measure a coastline's length, the total length equals the ruler size  $r$  times the number of steps of size  $r$ ,  $N(r)$ , taken in tracing the coast

$$L = rN(r) . \quad (2.5)$$

As with the snowflake,  $N(r)$  varies on the average as  $\frac{1}{r^D}$  and

$$L \propto r \frac{1}{r^D} = \frac{1}{r^{D-1}} . \quad (2.6)$$

With  $D > 1$ , as the size of the ruler used to measure a coast decreases, its length increases [1, 3]. The property that objects can look statistically similar while at the same time different in detail at different length scales, is the central feature of fractals in nature [3, 4].

A self-similar fractal set  $S$  is composed of  $N$  copies of itself (with possible translations and rotations) each of which is scaled down by the ratio  $r$  in all  $E$  coordinates from the whole.  $S$  here is the union of  $N$  distinct subsets each of which is congruent to  $rS$  [18].

A statistically self-similar fractal set  $S$  is one which is composed of  $N$  distinct subsets each of which is scaled down by the ratio  $r$  from the original and is identical in all statistical respects to  $rS$  [18].

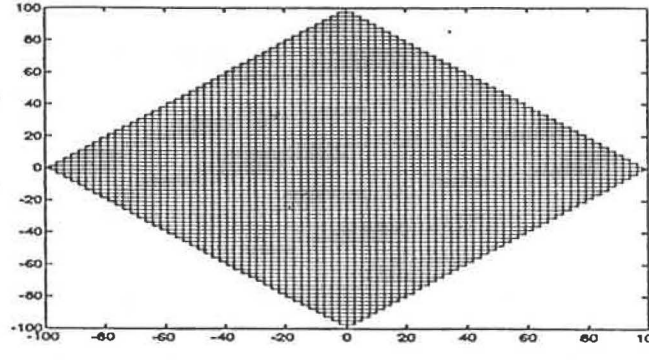
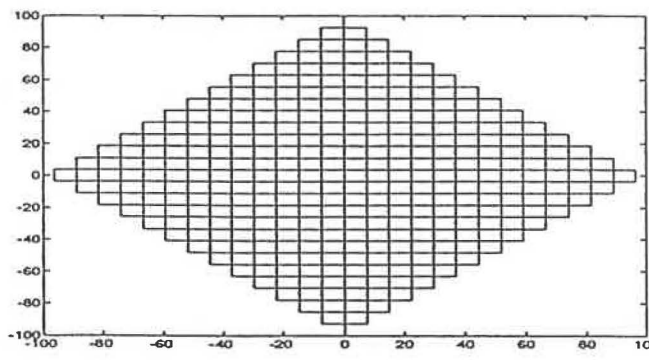
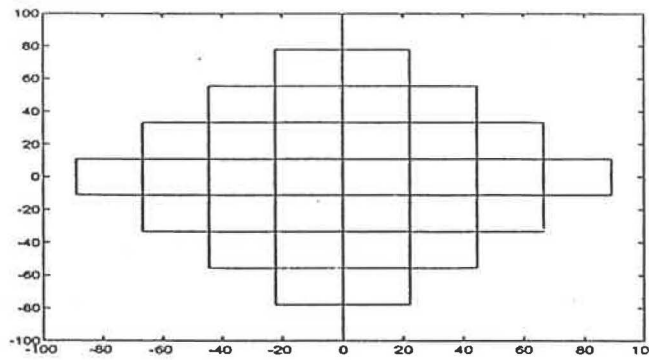
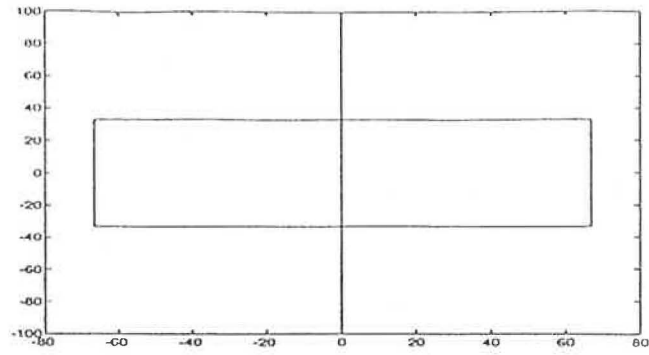


Figure 2.2. Four iterations of the Peano space filling curve

Similarly a bounded set  $S$  is self-affine when  $S$  is the union of  $N$  distinct subsets each of which is congruent to  $r(S)$  if the set  $S$  is transformed to  $r(S)$  where  $r=(r_1, \dots, r_E)$ .  $S$  is statistically self-affine when  $S$  is the union of  $N$  distinct subsets each of which is congruent in distribution to  $r(S)$  [18].

### 2.2.1. Fractal Dimension : Definition

There are several fractal dimensions which are capable of quantifying the degree of fragmentation of curves. They are:

1. The Hausdorff-Besicovitch Dimension ( $D_H$ ) .
2. The Minkowski-Bouligand Dimension ( $D_M$ ).
3. The Box counting Dimension ( $D_B$ ).
4. The Entropy Dimension ( $D_E$ ).

Mandelbrot [1] defines the fractal dimension as  $D_H$ . In order to give a measure of the size of a set of points,  $S$ , in space a test function  $h(\delta) = \gamma(d)\delta^d$  (a line, disk, ball or cube) is taken and is used to cover the set to form the measure  $M_d = \sum h(\delta)$ . For lines, squares and cubes the geometrical factor  $\gamma(d)=1$ . For disks, it is  $\frac{\pi}{4}$  and for spheres, it is  $\frac{\pi}{6}$ . In general, as  $\delta \rightarrow 0$ , the measure  $M_d$  is either zero or infinity depending on the choice of  $d$  which is the dimension of the measure. The Hausdorff-Besicovitch dimension  $D_H$  of the set  $S$  is the critical dimension for which the measure  $M_d$  changes from zero to infinity [19]:

$$M_d = \sum \gamma(d)\delta^d = \gamma(d)N(\delta)\delta^d \xrightarrow{\delta \rightarrow 0} \begin{cases} 0, d > D_H; \\ \infty, d < D_H. \end{cases} \quad (2.7)$$

The value of  $M_d$  which is called the  $d$ -measure of the set for  $d = D_H$  is normally finite but may be zero or infinite; it is the position of the jump in  $M_d$  as a function of  $d$  that is important.

For estimating the Minkowski-Bouligand dimension, the fractal curve is dilated with disks of radius  $\epsilon$  by forming the union of these disks centered at all points of the set thus creating a Minkowski cover. If  $A(\epsilon)$  is the area of the dilated set at all scales  $\epsilon$ , the infinitesimal order of  $A$  is

$$\lambda(A) = \lim_{\epsilon \rightarrow 0} \frac{\log A(\epsilon)}{\log \epsilon} . \quad (2.8)$$

The dimension  $D_M$  is  $2 - \lambda(A)$ .

For the box counting dimension, the plane is partitioned with a grid of squares of side  $\epsilon$  and the number of squares  $N(\epsilon)$  that intersect the curve are counted. The box dimension is obtained by replacing the Minkowski cover area with the box cover area

$$\epsilon^2 N(\epsilon) \text{ and is equal to } \lim_{\epsilon \rightarrow 0} \frac{\log N(\epsilon)}{\log \frac{1}{\epsilon}} .$$

For the entropy dimension, the curve is covered by disks of radii  $\epsilon$  and the dimension is computed as  $\lim_{\epsilon \rightarrow 0} \frac{\log N_{\min}(\epsilon)}{\log \frac{1}{\epsilon}}$  where  $N_{\min}(\epsilon)$  is the smallest number of such disks.

In general,  $0 \leq D_T \leq D_H \leq D_M = D_B \leq 2$  for a curve.

According to Mandelbrot [1],  $D_M$  is generally less desirable than  $D_H$ . But it is often identical to  $D_H$  and is easier to evaluate, hence it is useful. In general,  $D_M$  can be more robustly estimated than  $D_B$  [24]. It is shown in [51] that  $D_E = D_B$ . Falconer [51] gives a good mathematical description. In general,  $D_H$  is almost impossible to estimate in practical cases.

## CHAPTER 3

### FRACTIONAL BROWNIAN MOTION

Fractional Brownian motion (FBM) which is a generalization of ordinary Brownian motion has been shown to be useful in the analysis of time series data and in describing natural phenomena such as characterization of textures.

FBM is a non-stationary self-affine random process [1, 2] defined as:

$$B_H(t) - B_H(0) = \frac{1}{\Gamma(H+.5)} \left[ \int_{-\infty}^0 [(t-s)^{H-.5} - (-s)^{H-.5}] dB(s) + \int_0^t (t-s)^{H-.5} dB(s) \right] \quad (3.1)$$

where  $B(t)$  is Brownian motion and  $H$  is the Hurst Coefficient  $H$  ( $0 < H < 1$ ).

$H$  describes the roughness of the curve  $B(t)$  and the value of  $D$  for the graph will be  $2-H$  [2].  $H$  relates the incremental change in  $B$  to the time difference:

$$\Delta B(t) \propto (\Delta t)^H . \quad (3.2)$$

Both ordinary and fractional brownian motions have variances of increments that diverge with time [19]. In FBM, past increments are correlated with future increments and it has infinitely long run coefficients [19].

Given the increment  $B_H(0) - B_H(-t)$  from  $-t$  to  $0$  the probability of having an increment  $B_H(t) - B_H(0)$  averaged over the distribution of past increments is

$$\langle [B_H(0) - B_H(-t)][B_H(t) - B_H(0)] \rangle . \quad (3.3)$$

Assuming  $B_H(0) = 0$  the correlation function of future increments  $B_H(t)$  with past increments  $-B_H(-t)$  may be written as:

$$C(t) = \frac{\langle -B_H(-t)B_H(t) \rangle}{\langle B_H(t)^2 \rangle} = 2^{2H-1} - 1 . \quad (3.4)$$

For  $H = \frac{1}{2}$ , the correlation of past and future increments  $C(t)$  vanishes for all  $t$  as is required for an independent random process. This is as expected as at  $H = \frac{1}{2}$ , FBM is the same as ordinary brownian motion. For  $H \neq \frac{1}{2}$  we have  $C(t) \neq 0$ , independent of  $t$ . For  $H > \frac{1}{2}$  we have persistence which means that if for some time in the past we have an increase, we also on the average have an increase in the future. Conversely, a decreasing trend in the past implies on the average a continued decrease in the future. For  $H < \frac{1}{2}$  we have anti-persistence in which an increasing trend in the past implies a decreasing trend in the future and vice versa.

It has been shown [2] that the Power Spectral Density (PSD) of FBM is related to the frequency as

$$S(f) = f^{-(2H+1)} . \quad (3.5)$$

Flandrin [23] describes the spectrum of FBM based on time frequency analysis as well as time scale analysis.

FBM is a time varying process but the increments of FBM known as Fractional Gaussian Noise (FGN) form a strict sense stationary process [2].

The properties of FGN are [2] :

1. It is a zero mean process.
2. It is a strict sense stationary process.
3.  $Var[B(t_2; H) - B(t_1; H)] = V_H (t_2 - t_1)^{2H}$  where  $V_H$  is the variance given by

$$V_H = \frac{1}{\Gamma(H+0.5)^2} \left[ \int_{-\infty}^0 \{(1-s)^{H-0.5} - (-s)^{H-0.5}\}^2 ds + \frac{1}{2\pi} \right] \quad (3.6)$$

$$4. \Pr \left\{ \frac{B(t_2; H) - B(t_1; H)}{(t_2 - t_1)^H} < y \right\} = F(y)$$

where  $F(y)$  is a cumulative Gaussian distribution function with zero mean.

5.  $B(t+k; H) - B(t; H)$  is distributed identically as  $h^{-H} [B(t+kh; H) - B(t; H)]$

The power spectrum of FGN [2] [23] can be written as:

$$S(f) = kf^{-(2H-1)}. \quad (3.7)$$

Discrete FBM (DFBM) and Discrete FGN (DFGN) are the sampled versions of FBM and FGN. DFGN  $X[]$  is a strict sense stationary zero mean process with a correlation structure

$$r[k] = \frac{\sigma^2}{2} [ |k+1|^{2H} - 2|k|^{2H} + |k-1|^{2H} ] \quad (3.8)$$

where  $\sigma^2$  is the variance of  $X[]$ ,  $r[k] = E\{X[n+k; H]X[n; H]\}$  and  $X[k; H] = B[k; H] - B[k-1; H]$ . This can be shown by considering  $r[k] = E\{X[n+k]X[n]\} = E\{(B[n+k+1] - B[n+k])(B[n+1] - B[n])\}$  where the second arguments have been dropped. This can be written as :

$$r[k] = \frac{1}{2} \{ E[(B[n+k+1] - B[n+k])^2] + E[(B[n+k] - B[n])^2] - E[(B[n+k+1] - B[n+1])^2] - E[(B[n+k] - B[n])^2] \}$$

to which the direct application of the property 3 of FGN gives Equation 3.8.

## CHAPTER 4

### GENERATIVE METHODS

Various generative methods have been developed with varying degrees of complexities for FBM generation [18, 27, 38]. Four popular methods have been used to generate FBM so that the performance of the estimators of H can be compared.

The generative methods used are:

1. Midpoint Displacement,
2. Spectral Synthesis,
3. Weierstrass-Mandelbrot Formula, and
4. Cholesky Decomposition.

#### 4.1. Midpoint Displacement method

This method is described in detail in reference [18] and makes use of the property of FBM  $Var(B(t_2) - B(t_1)) = |t_2 - t_1|^{2H} \sigma^2$  and the midpoint displacements are

$D_n$  that have variances  $\Delta_n^2 = \frac{\sigma^2}{(2^n)^{2H}} (1 - 2^{2H-2})$ . Although this process produces a

fractal, it is not stationary for all H [18]. FBM samples of length 256 were generated for different values of H. Figure 4.1 shows FBM samples for H=0.1, 0.4 and 0.9. Figure 4.2 shows the corresponding FGN samples. As expected the FBM graph for H=0.9 is very smooth and the one for H=0.1 is rough and the one for H=0.4 shows the transition. The FGN samples do not differ much from each other. Figures 4.3 and 4.4 are the corresponding figures in the presence of noise at 30 db. The noise adds fragmentation to the FBM curves.

#### 4.2. Spectral Synthesis

This method uses the strict power law of the PSD of FBM (3.5). Hence, FBM samples can be obtained by constructing a random function with the desired spectral density. Assuming that the output of a pseudo-random number generator produces a white noise  $W(t)$ , filtering  $W(t)$  with a transfer function  $T(f)$  produces an output  $V(t)$  whose spectral density is:

$$S_v(f) \propto |T(f)|^2 S_w(f) \propto |T(f)|^2 . \quad (4.1)$$

Thus to generate a  $\frac{1}{f^\beta}$  noise from a  $W(t)$  process requires  $T(f) \propto \frac{1}{f^{\frac{\beta}{2}}}$ . Hence

a reasonably good approximation to FBM can be obtained by multiplying the Fourier coefficients of a white noise sequence by  $\frac{1}{f^{\frac{\beta}{2}}}$ . To avoid the periodicity inherent in

the FFT and to offset boundary constraints a longer sequence was generated and a truncated portion of it was used. Extending the same concept to two dimensions, fractal surfaces can be produced by multiplying the Fourier coefficients of a two-dimensional

white noise matrix by  $\frac{1}{(f_x^2 + f_y^2)^{\frac{\beta+1}{2}}}$ . Figure 4.5 shows  $64 \times 64$  fractal brownian surfaces

generated using this method for  $H=0.11$ ,  $0.4$  and  $0.99$ . As expected, the surface for  $H=0.99$  is very smooth and the one for  $H=0.11$  is very rough and the surface for  $H=0.4$  shows the transition.

#### 4.3. Weierstrass Sine function

The Weierstrass Sine function is a parametric fractal signal and is the imaginary part of the Weierstrass-Mandelbrot fractal function [34].

$$W(t) = \sum_{n=-\infty}^{n=+\infty} \frac{(1 - e^{i\gamma^n t}) e^{i\phi_n}}{\gamma^{(2-D)n}} \quad (1 < D < 2, \gamma > 1, \phi_n = \text{arbitrary phases}) \quad (4.2)$$

which is continuous everywhere but differentiable nowhere.

The function  $W(t)$  possesses no scale and the graph has a fractal dimension  $D = 2 - H$  [34]. Since  $W$  is complex both the real and imaginary parts of it exhibit these properties.  $\gamma$  is a parameter and the phases  $\phi_n$  can be chosen to make  $W(t)$  exhibit deterministic or stochastic behavior. Taking the imaginary part of  $W(t)$  we can write the following fractal function:

$$W_1(t) = \sum_{n=-\infty}^{n=+\infty} G_n \gamma^{nH} \sin(2\pi\gamma^{-n}t + \phi_n) \quad (4.3)$$

where  $G_n$  is a Gaussian random variable with the same variance for all  $n$  and  $\phi_n$  is a random phase uniformly distributed in  $0 - 2\pi$ . The spectral density of  $W_1$  can be shown to be proportional to  $1/f^{(2H+1)}$  [34]. A point to be noted here is that  $W_1$  has  $D$  as a box dimension, but only approximately as Hausdorff-Besicovitch dimension [19].

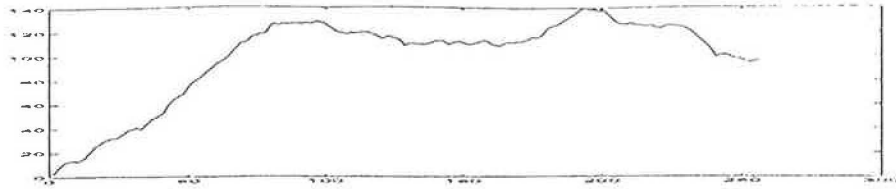
#### 4.4. Cholesky Decomposition method

As described by reference [38], to generate FBM samples independently, it is preferable to uncorrelate the samples by a transform, realize the samples and transform back again to get the covariance matrix. Using Cholesky decomposition [35], the covariance matrix  $R$  can be written as:

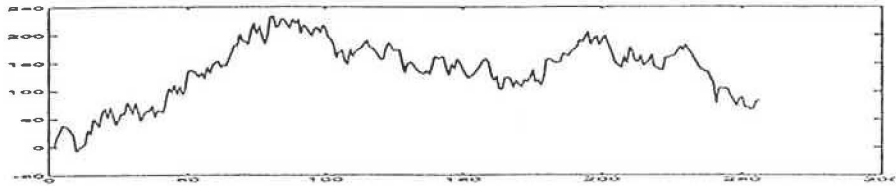
$$R = LL^T. \quad (4.4)$$

The samples can be realized as  $X$  where  $X = LY$  and  $Y$  is a Gaussian distributed vector.

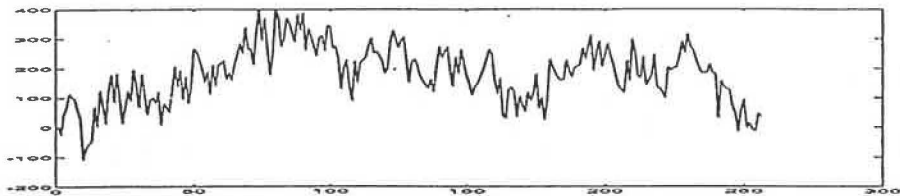
Even though computationally more complex than the other approaches, this rigorous approach produces a very good approximation to FBM.



$H = 0.9$

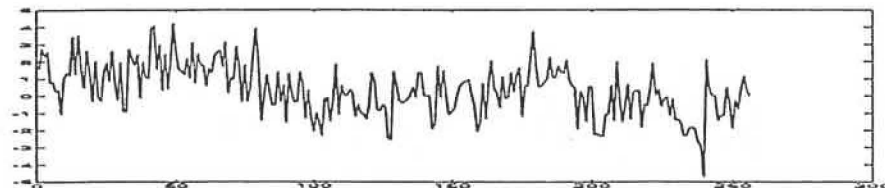


$H = 0.4$

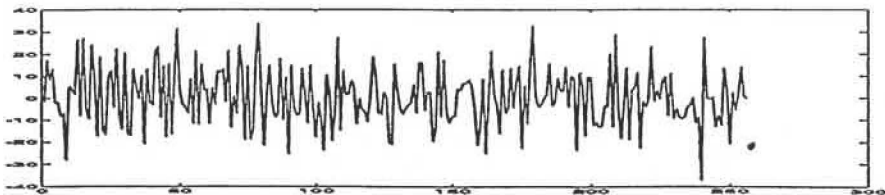


$H = 0.1$

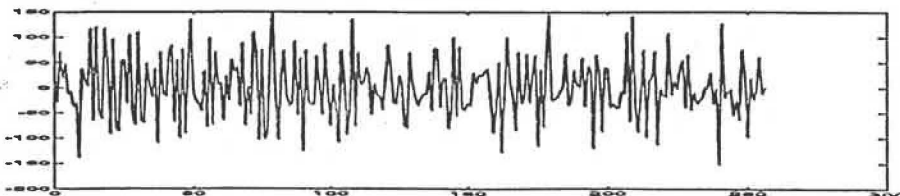
Figure 4.1 FBM for H



$H = 0.9$

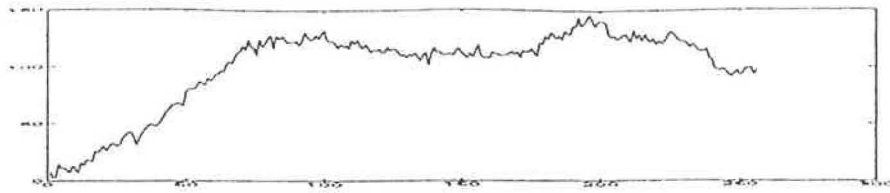


$H = 0.4$

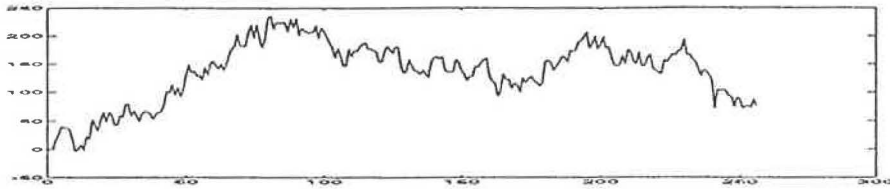


$H = 0.1$

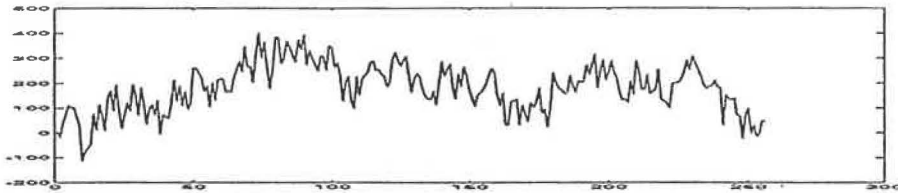
Figure 4.2 FGN for H



H = 0.9

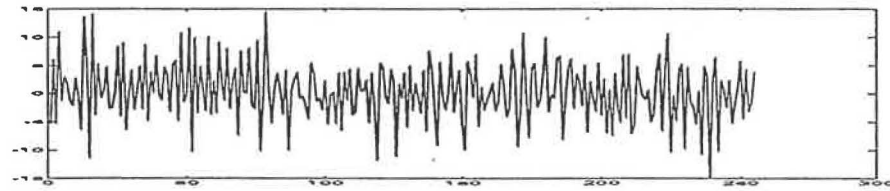


H = 0.4

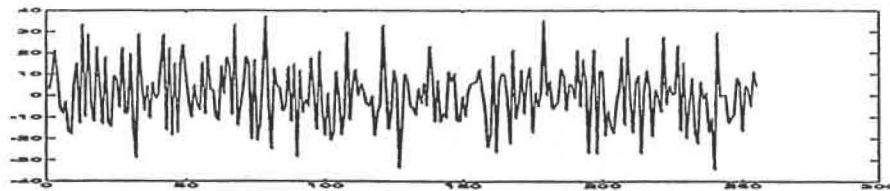


H = 0.1

Figure 4.3 FBM for H with S/N 30 db



H = 0.9

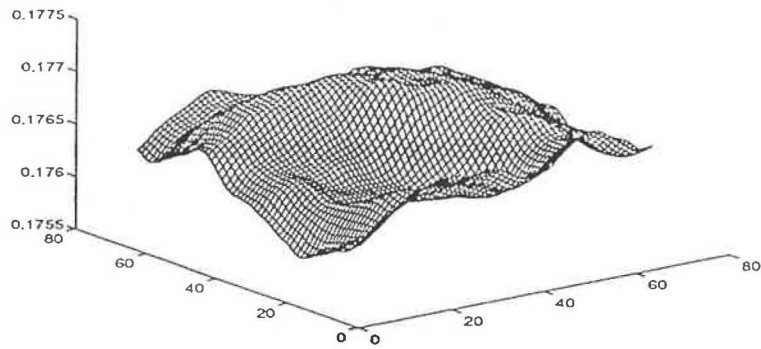


H = 0.4

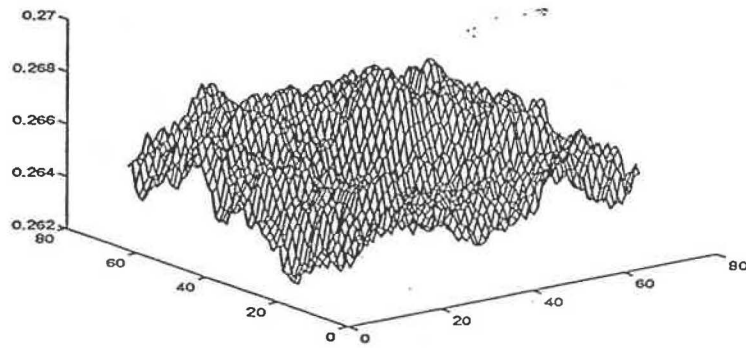


H = 0.1

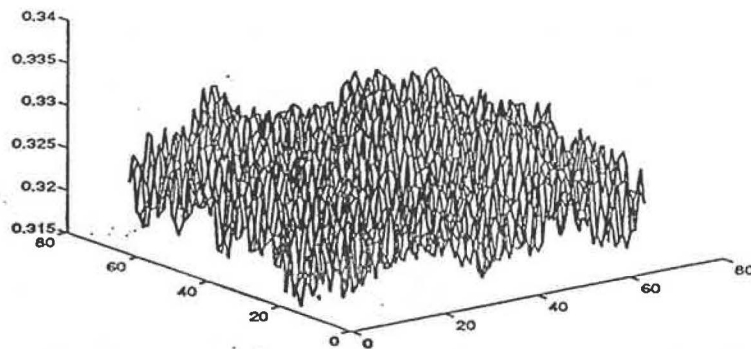
Figure 4.4 FGN for H with S/N 30 db



$H = 0.99$



$H = 0.4$



$H = 0.11$

Figure 4.5 Fractal Brownian surfaces

## CHAPTER 5

### ESTIMATION METHODS

#### 5.1. Introduction

The methods used to measure  $H$  for FBM signals can be classified as :

1. Methods exploiting the PSD law of FBM,
2. Methods using the self-affinity properties of FBM, and
3. Maximum Likelihood Estimation methods.

The PSD method is popular because of the simplicity of computing spectra using FFT. This has been improved by the use of Gabor filters (for the 2-D case) by Bovik and Super [46] and also by using wavelet decomposition [25]. The relationship between the dimension and the power law index and the problems therein were investigated by Higuchi [26]. This method has been applied to texture analysis [13, 16, 46].

The methods using the self-affinity properties exploit the property of the power law of its moments. This method also is fairly robust [14] and has been successfully applied to texture analysis [42].

The MLE method is shown to be asymptotically efficient and asymptotically optimal as it attains the Cramer-Rao lower bound [38, 39]. Reference [38] reports degraded performance in the noisy case. Ogata et al. [21] obtain the spectral likelihood estimate (based on the distribution of the periodogram) of the fractal dimension for random point patterns and planar curves.

In addition to these methods Maragos [10, 24] estimates the fractal dimension of time series data using morphological covers and iterative optimization and reports good results for estimating the Minkowski-Bouligand dimension.

## 5.2. PSD of FGN

This estimation method uses the strict power law of the PSD of FBM [2]. As DFGN is the process formed by the increments of DFBM, the PSD of FGN is given by Equation 3.7. From this we can write:

$$\log(S_v(f)) = -(2H - 1)\log(f) + \log(k) . \quad (5.1)$$

Hence, the slope of a least squares straight line fit of the log-log plot of the PSD versus frequency gives the estimate of the fractal dimension. Different window functions were tried but the differences in the estimates were negligible. The results shown in the tables are for a Hamming window.

## 5.3. Relative Dispersion

This method makes use of the dependence of the variance of a variable on the resolution. The RD analysis method compares the variance of a variable as the measurement resolution increases. The RD coefficient equals the ratio of the standard deviation and the mean. At the highest level of resolution, the variance of the signal over its whole length is measured. After that the signal is averaged over increasing number of consecutive values and the variance measurements are taken for each case. Bin sizes taken here are 2, 4, 8, 16 and 32. The mean should remain the same. If the signal is white noise, the standard deviation should decrease by  $\frac{1}{n^{0.5}}$  if  $n$  is the bin size or time resolution interval. But for a fractal signal

$$RD = RD_r \left(\frac{n}{n_r}\right)^{(H-1)} \quad (5.2)$$

$$\log(RD) = (H - 1)\log\left(\frac{n}{n_r}\right) + \log(RD_r) . \quad (5.3)$$

where  $RD_r$  is RD for the reference bin size  $n_r$  [20, 28]. The slope of the least squares straight line fit of the log-log plot of the RD coefficient versus  $n$  will give the value of  $H$ .

RD analysis is especially suited for short signals as the first four components mainly determine the slope of the graph. Because of the averaging inherent in the algorithm it is suitable for noisy signals too. In addition to this it is not demanding computationally.

#### 5.4. Maximum Likelihood Estimation

##### 5.4.1. Introduction

The theory of statistical inference [31, 32], consists of two parts, tests of significance and estimation theory. In a test of significance, a given set of data is examined to see whether it is consistent or not consistent with a specific hypothesis about a random variable. In estimation theory, the data is used to estimate the values of the parameters in some assumed probability density function for the random variable and to determine the accuracy of the estimates.

##### 5.4.2. Maximum Likelihood Estimation

Let  $x_1, \dots, x_n$  be a set of  $n$  independent random samples drawn from a given population. The population is characterized by a probability density function  $f_n(x; \theta) = f_n(x_1, \dots, x_n; \theta)$ .  $\theta$  is a parameter of the population distribution. The likelihood function  $L$  is defined in this case by the relation:

$$L(x_1, \dots, x_n; \theta) = f_n(x_1, \dots, x_n; \theta) = \prod_{i=1}^n f(x_i; \theta) . \quad (5.4)$$

If the population consists of discrete elements, the likelihood function is

$$L(x_1, \dots, x_n; \theta) = \prod_{i=1}^n p_i(\theta), \quad (5.5)$$

where  $p_i(\theta)$  is the probability associated with the  $i$  th sample.

When the sample values are given as well as the functional form of the population probability density function, the likelihood function can be regarded as a function of the distribution parameter  $\theta$ . The method of maximum likelihood is one of selecting an estimate  $\hat{\theta}$  for  $\theta$  which will maximize the likelihood function [29, 30]. Since the logarithm is a monotonic function, the solution to the MLE problem can be obtained by:

$$\frac{\partial}{\partial \theta} \log(L) = 0 = \frac{\partial}{\partial \theta} \sum_{i=1}^n \log(f(x_i; \theta)). \quad (5.6)$$

Any solution  $\hat{\theta}$  for  $\theta$  which satisfies [5.6] and is not identically a constant is called an ML Estimate of  $\theta$ . Equation [5.6] is called the likelihood equation.

#### 5.4.3. Application of MLE to DFGN

Since the samples of FGN are jointly Gaussian distributed, the probability density function of DFGN can be written as

$$P(x; H) = \frac{1}{(2\pi)^{\frac{N}{2}} |R|^{0.5}} e^{[-0.5 \cdot x^T R^{-1} x]} \quad (5.7)$$

where  $x$  is the dataset and  $R$  is the covariance matrix which can be obtained from the autocorrelation function [33] as

$$[R]_{ij} = r[|i - j|]. \quad (5.8)$$

The MLE is considered to be an optimal estimator as the estimate is asymptotically unbiased and asymptotically efficient and it obtains the Cramer-Rao bound [38, 39].

The objective is to find the value of  $H$  that maximizes  $P(x;H)$ . Since the logarithm is a monotonic function, the log of  $P(x;H)$  can be maximized instead of  $P(x;H)$  itself. The log likelihood function can be written as

$$\log(P(x;H)) = \frac{-N}{2} \log(2\pi) - \frac{1}{2} \log|R| - \frac{1}{2} x^T R^{-1} x . \quad (5.9)$$

Writing  $R = \sigma^2 R_1$  the likelihood function can be written as:

$$\log(P(x;H)) = \frac{-N}{2} \log(2\pi) - \frac{N}{2} \log(\sigma^2) - \frac{1}{2} \log|R_1| - \frac{1}{2} x^T R_1^{-1} x \quad (5.10)$$

which can be minimized over  $\sigma^2$ .

This yields  $\sigma^2 = \frac{x^T R_1 x}{N}$ . The final likelihood function which has to be maximized

$$\text{over } H \text{ is } \log(P(x;H)) = \frac{-N}{2} \log(2\pi) - \frac{N}{2} \log \frac{(x^T R_1 x)}{N} - \frac{N}{2} - \frac{1}{2} \log|R_1| \quad (5.11)$$

Levinson-Durbin algorithm [35] can be used to decompose  $R_1$ . This simplifies the MLE solution. Then the golden search method [35] yields the maximization result.

#### 5.4.4. MLE for noisy data

Reference [38] reports degraded performance in the presence of noise. It is proposed in references [38] and [39] that the noise should be either filtered out or included in the estimation model.

An attempt was made to study the effect of noise on the data and on the performance of the MLE. It was suspected that the noise might be affecting the distribution of the samples. Hence non-parametric tests [29] were used on the data sets to detect the degraded performance and to specify the noise level at which the performance is unacceptable by studying the distribution. The tests used were the Lilliefors test [29, 36], and the Cramer-Von Mises test [29, 37].

#### 5.4.4.1. Lilliefors test

Let the data consist of a random sample  $x_1, \dots, x_n$  of size  $n$  associated with some unknown distribution function, denoted by  $F(x)$ . Computing the sample mean and variance, the normalized sample values  $z_i$  can be computed as  $z_i = \frac{x_i - \bar{x}}{s}$  where  $\bar{x}$  and  $s$  are the sample mean and standard deviation. The test statistic is computed from the  $z_i$  s instead of from the original sample. The assumption is that the sample is a random one. The hypotheses are :

$H_0$  : The random sample has the normal distribution, with unspecified mean and variance.

$H_1$  : The distribution function is non normal.

The test statistic is the two sided Kolmogorov test statistic, which is the maximum vertical distance between the empirical distribution function of the  $x_i$  s and the normal distribution function. In other words the Lilliefors test statistic  $T$  is defined by:

$$T = \sup_x |f^*(x) - S(x)| \quad (5.12)$$

where  $f^*(x)$  is the standard normal distribution and  $S(x)$  is the empirical distribution function.

The decision rule is : Reject  $H_0$  at the approximate level of significance  $\alpha$  if  $T$  exceeds the  $1-\alpha$  quantile as given in the table in Appendix B.

#### 5.4.4.2. Cramer-Von Mises test

This goodness of fit statistic is given by:

$$w_N^2 = N \int_{-\infty}^{\infty} [F_n(x) - F_0(x)]^2 dF_0(x) = \frac{1}{12N} + \sum_{i=1}^N \left[ F_0(x_i) - \frac{(2i-1)}{2N} \right]^2 \quad (5.13)$$

where  $F_N(x)$  is the empirical cumulative distribution function,  $N$  is the sample size and  $x_1 \leq \dots \leq x_n$  are the sample values [37]. The decision rule is the same as before and the table is given in Appendix A. Even though degradation of performance was observed at S/N 20 db and below, the tests failed to produce any level of significance which might be fixed after which the MLE fails. It can also be observed (from the tables 6.1-6.5) that the percentage errors of estimation are higher for higher values of  $H$ . It may be due to subtle changes in the long time correlation structure which cannot be detected in the statistical model. This effect may not be affecting the distribution of the data much but might make the MLE converge to a wrong estimate.

#### 5.4.5. MLE for the Gaussian Noise Model

The filtering of noise in this case is difficult as it may spoil the inherent roughness of the graph. If the noise is modeled as white Gaussian noise  $N[k]$ , as FGN is a Gaussian process and since the samples of noisy FGN are

$X_n[k] = B_n[k+1] - B_n[k]$  where  $B_n[k] = B[k] + N[k]$ , the noisy FGN is the sum of two Gaussian processes. The structure of the new covariance matrix  $R_n$  is  $R_n(i, j) = R(i, j) + N_n(i, j)$  where  $N_n$  is the noise covariance matrix.

This is simple to estimate from the knowledge of the noise process [33]. If no knowledge about the noise process is assumed, the search becomes a two dimensional maximization over  $H$  and variance of the noise. The computational effort for this case especially in applications like automated inspection of textured images, can be prohibitive.

## CHAPTER 6

### RESULTS FOR ONE-DIMENSIONAL DATA

All results are shown on FBM data sets of length 256. Table 6.1 shows the results of the estimation of  $H$  done on data sets generated using the midpoint displacement method. The fractal produced is not stationary for all  $H$ . Points generated at different stages have different statistical properties in their neighborhoods. The effect is more pronounced as  $H$  tends to 1. This may be the reason for the relatively higher error for the MLE.

Table 6.2 shows the results of the estimation on data sets generated using the Weierstrass Cosine formula. The MLE is not shown here as the data sets do not preserve a good Gaussian distribution and hence the MLE values are not very accurate. Table 6.3 shows the results on data sets generated from the SS method. The MLE values are not shown for the same reason mentioned before. The above two methods yield comparable performance for both these generative algorithms.

Table 6.4 shows the performance on data sets generated by the Cholesky Decomposition method. This method of FBM generation is a very rigorous one and the ability of the MLE can be demonstrated.

Table 6.5 shows the results of the estimation on noisy data sets. The robustness of the MLE in the presence of significant noise is shown.

It is proposed that the MLE be used for relatively short signals. When the data length becomes long; the computation load becomes large and the relative dispersion method can be used. A point to be mentioned here is that when a signal generating algorithm produces a signal with a different fractal dimension from the one corresponding to  $H$ , it cannot be expected that the estimation procedures will be

unbiased with respect to the present parameter value. Hence the generative algorithm even if computationally more complex should be a rigorous one.

Table 6.1. Results of estimation on data sets generated using Midpoint Displacement

Actual Values	MLE Values	Percent Error	PSD Values	Percent Error	RD Values	Percent Error
1.9	1.650	13.16	1.9119	0.63	1.8906	0.49
1.8	1.795	0.28	1.7890	0.61	1.7907	0.52
1.7	1.685	0.88	1.6770	1.35	1.6915	0.50
1.6	1.583	1.06	1.5853	0.92	1.5996	0.025
1.4	1.408	0.57	1.4224	1.60	1.4327	2.34
1.3	1.315	1.15	1.3244	1.80	1.3593	4.56
1.2	1.228	2.33	1.2213	1.86	1.2536	4.47
1.1	1.119	1.73	1.2220	2.02	1.2364	2.40

Table 6.2. Results of estimation on data sets generated using Weierstrass method

Actual Values	PSD Values	Percent Error	RD Values	Percent Error
1.9	1.791	5.79	1.8595	2.13
1.8	1.770	1.67	1.7878	0.68
1.7	1.631	4.06	1.6769	1.36
1.6	1.530	4.38	1.5804	1.23
1.4	1.297	7.36	1.3305	4.96
1.3	1.180	9.23	1.2414	4.51
1.2	1.092	9.00	1.1821	1.49
1.1	0.90	18.2	1.1121	1.10

Table 6.3. Results of estimation on data sets generated by Spectral Synthesis

Actual Values	PSD Values	Percent Error	RD Values	Percent Error
1.9	1.846	2.84	1.8389	3.22
1.8	1.822	1.22	1.8354	1.97
1.7	1.731	1.82	1.7469	2.76
1.6	1.625	1.56	1.6150	0.94
1.4	1.370	2.14	1.3760	1.71
1.3	1.282	1.38	1.2753	1.90
1.2	1.175	2.08	1.2150	1.25
1.1	1.1124	1.13	1.2050	9.55

Table 6.4. Results of estimation on data sets generated by Cholesky Decomposition

Actual Values	ML E Values	Percent Error	PSD Values	Percent Error
1.9	1.912	0.63	2.070	8.95
1.8	1.809	0.50	1.885	4.72
1.7	1.714	0.82	1.737	1.76
1.6	1.611	0.69	1.6563	3.52
1.4	1.415	1.07	1.3855	1.04
1.3	1.292	0.62	1.2675	2.50
1.2	1.208	0.67	1.2326	2.72
1.1	1.107	0.64	1.0677	2.94

Table 6.5. Results of estimation on noisy data sets generated by Cholesky Decomposition S/N=30db

Actual Values	ML E Values	Percent Error	PSD Values	Percent Error
1.9	1.936	1.89	1.96	3.16
1.8	1.821	1.17	1.60	11.0
1.7	1.727	1.59	1.8318	7.75
1.6	1.628	1.75	1.6701	4.38
1.4	1.472	5.14	1.5337	9.50
1.3	1.355	4.23	1.3393	3.02
1.2	1.404	17.0	1.5156	26.3
1.1	1.671	51.9	1.7918	62.9

## CHAPTER 7

### TEXTURE ANALYSIS

#### 7.1. Introduction

Texture classification and analysis play an important role in image processing and computer vision. Besides being an intrinsic feature of realistic objects, texture gives important information on depth and orientation of an object. Most existing texture recognition approaches can be broken down into components which are based on statistical or structural properties of the image [40]. The statistical approach assumes that second-order probability distributions are enough for human discrimination of two texture patterns. Structural approaches describe a texture by rules governing the placement of the primitive elements of the texture. These primitives are local patterns of varying or standard shapes and they form the texture by certain placement rules such as orientation and size [43]. In the stochastic formulation, texture is considered as a sample from a probability distribution on the image space [44]. The image space is an  $N \times N$  grid and each grid point is considered as a random variable in the range {0-256}. Features of the stochastic and deterministic viewpoints have been combined in "mosaic" models [45] which involve repetition of random pattern generation processes in order to provide image structure.

Rao [49] provides a taxonomy for texture description where textures are divided into Strongly Ordered, Weakly Ordered and Disordered textures. The textures for which a statistical model is appropriate are classified as Disordered textures. They show neither repetitiveness nor orientation and can be described by a roughness measure. Textures which are amenable to structural description by virtue of repetitiveness are classified as Strongly Ordered. Textures which are characterized by a dominant local orientation at each point of the texture which can vary arbitrarily are Weakly Ordered.

Disordered textures can be effectively described by the concept of surface roughness and the fractal model is especially suitable for this description [14, 49]. In addition to this, Pentland [14] has shown that the fractal dimension correlates well with a human's assessment of surface roughness.

## 7.2. Fractal Characterization of Textures

Several papers have been devoted to fractal brownian model for texture analysis led by Pentland [14, 15, 16, 17]. Pentland shows the use of fractal modeling not only in texture classification and segmentation but also in obtaining shape estimates. Nguyen and Quinqueton [11] had already shown texture analysis based on the irregularities of space filling Peano curves [1] obtained by transforming windows of 2-D surface images to 1-D Peano curves. Medioni and Yasumoto [42] mention some problems encountered during texture classification by fractal modeling and compare the segmentation achieved with the model to one using conventional intensity based method. Peleg et al. [41] derived a set of features based on the  $\epsilon$ -blanket method and used these as global characteristics to recognize large texture patches. Keller and Chen [47] use the concept of lacunarity along with the fractal dimension to describe and segment natural texture images. Super and Bovik [46] used Gabor filters for obtaining accurate localized measurements of the fractal dimension. Dennis and Dessipris [48] suggest the idea of differentiating locally determined fractal dimensions and call it the D-signature of the texture. Sarkar and Chaudhuri [57] describe an efficient covering method to compute the fractal dimension of textures.

In this thesis we try to characterize natural textures using the fractal brownian surface model. A surface is fractal if the fractal dimension is stable over a wide range of scales. According to Pentland, "A 3-D surface with a spatially isotropic fractal brownian shape produces an image whose fractal dimension is identical to that of the

components of the surface normal, given a Lambertian surface reflectance function and constant illumination and albedo" [14].

### 7.2.1. Texture Classification

Initially single texture homogenous polymer membrane images have been modeled as images formed from a fractal Brownian surface. Each of these is  $128 \times 128$  pixels digitized to 8 bits. Figure 7.1 shows the distributions of intensity differences at one, two, four and eight pixel distances for a sample texture path and it can be observed that they are approximately Gaussian distributed. Hence we can assume that the intensity surface is approximated by a FBM function at least over the 8:1 range of scales measured. The fractal dimension was computed in  $16 \times 16$  windows with an increment of 4 pixels between the windows. Within each window, line to line formulation is used and the fractal dimension is normally the average of the values obtained from the rows and the columns. Another method in which the mode of the values gives the fractal dimension was tried. If two high frequency components were found, the average was taken. This method yielded better results for the textures used and the results presented are for this method. This method is particularly useful for natural textures as they may have one or two values of  $H$  within each window described previously which are totally different from the ones obtained from the other rows and columns. In such cases this method ensures that the value that occurs the most is the one representing the texture patch as averaging may introduce errors here:-The histograms of the fractal dimensions should show ideally a single peak at one value of the fractal dimension. But as the real images are an approximation to a fractal brownian surface, a spread is invariably seen around the peak. The texture is shown in Figure 7.2. The histogram values plotted are for  $D_1 = 128 - 50H$  for clarity (Figure 7.3). It can be seen that the texture is characterized well by the value of  $H$  by looking at the histogram.

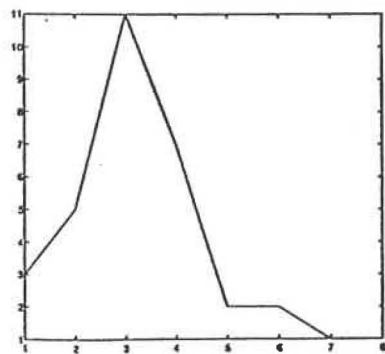
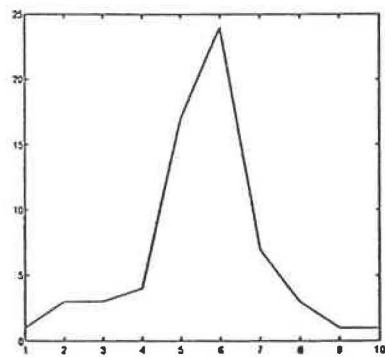
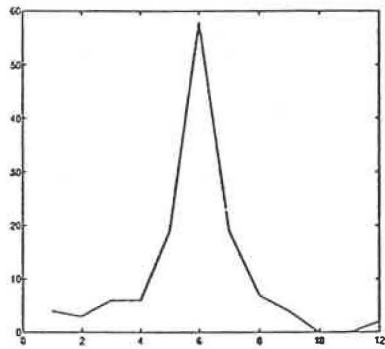
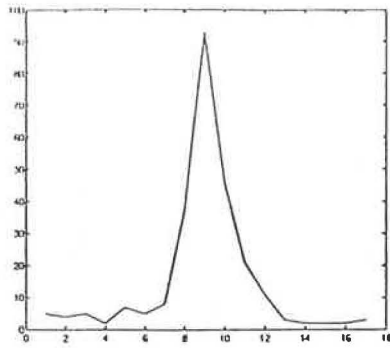


Figure 7.1 Histograms of pixel differences for a typical textured path. Differences are 1, 2, 4 and 8.

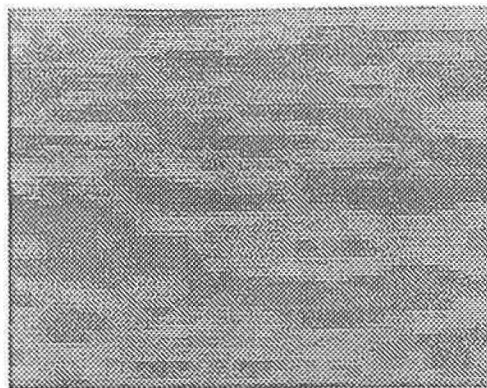


Figure 7.2 Single homogenous texture polymer image

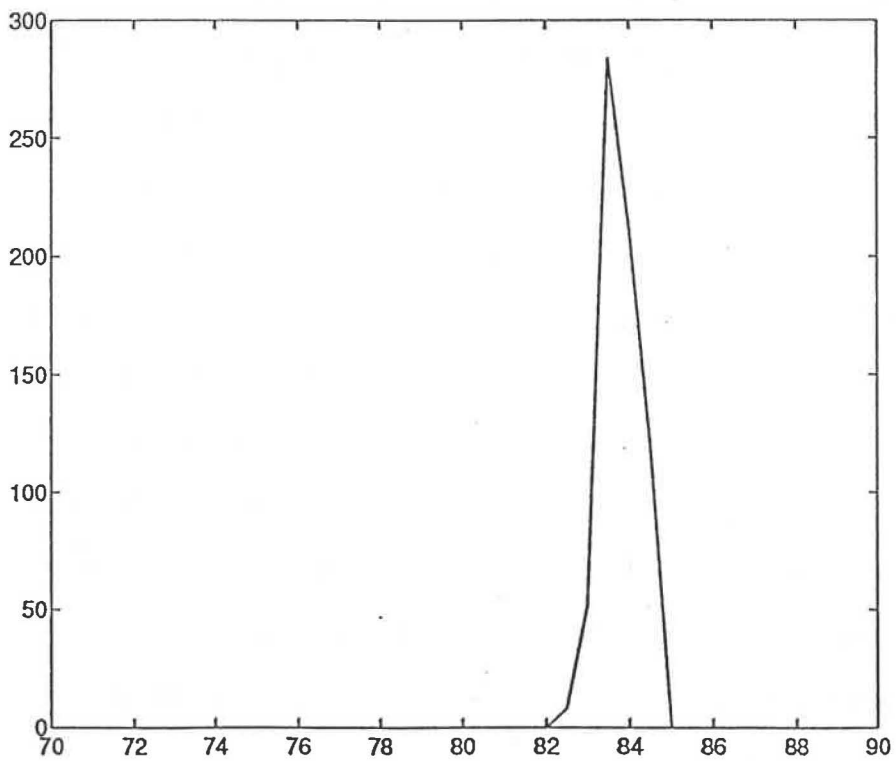


Figure 7.3 Histogram of fractal dimensions for the homogenous texture image

Texture images from the Brodatz album [58] were selected for testing the characterization. Figure 7.4 shows a single homogenous texture from the album (Burlap). The histogram of fractal dimensions for this is shown in the Figure 7.5. It has a single peak with a slight spread around the peak and hence it can be concluded that the texture is characterized by its fractal dimension.

### 7.2.2. Texture Segmentation

Texture segmentation is an important step in the analysis and interpretation of scenes in machine vision applications, satellite imagery, etc. Texture segmentation is achieved by the process of feature extraction, followed by segmentation based on classification of these features [56]. Segmentation algorithms are typically divided into region-based and boundary-based algorithms. Reference [56] describes the problem of texture segmentation and discusses the shortcomings of region-based and boundary-based approaches. To demonstrate the ability of the method to segment textures, four homogenous regions were taken from the images of the polymer membranes. The composite image is  $128 \times 128$  pixels digitized to 8 bits (Figure 7.6). As explained before the fractal dimension was computed in  $16 \times 16$  windows with an increment of 4 pixels between windows leading to a  $32 \times 32$  pixel picture. Since the composite image contains four different textures, the edges of the textures pose a problem. One way to solve it is to detect the edges initially and then compute the dimension within the edges. The other way is to detect the edge by noting that the fractal dimension will be less than the topological dimension in such cases. Hence  $H$  is not in the range of 0 to 1 and the texture edge is detected. The histogram of the fractal dimensions should ideally give four peaks corresponding to the dimensions of each of the textures. But as said before as these are only approximately fractal brownian surfaces, there is a spread around the peaks of the histogram. In addition to this, two of the textures had closely

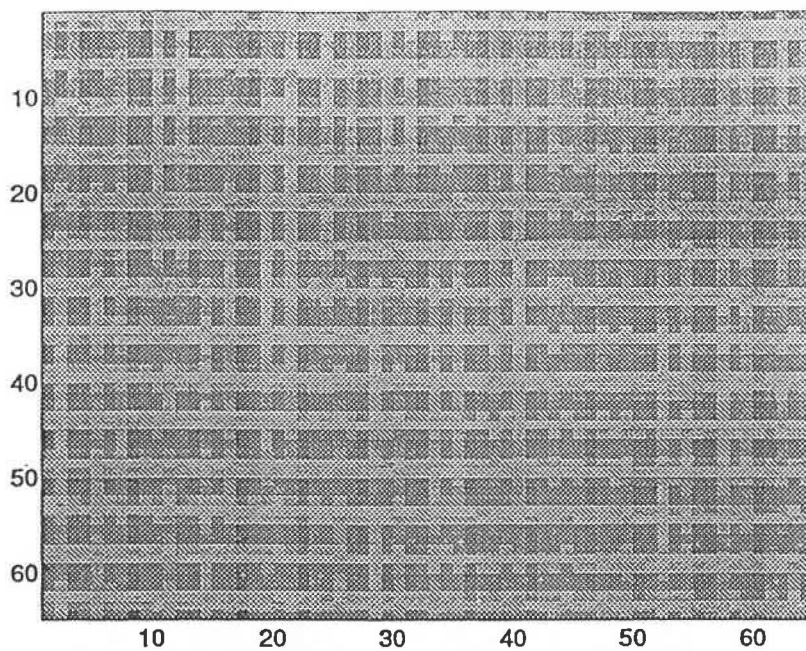


Figure 7.4 Homogenous Brodatz texture (Burlap)

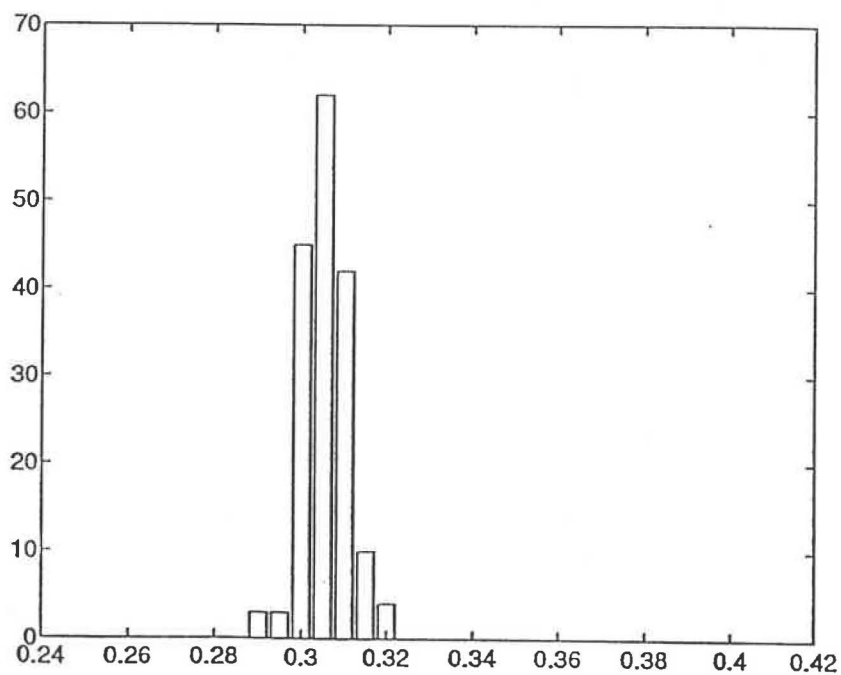


Figure 7.5 Histogram of fractal dimensions for Burlap

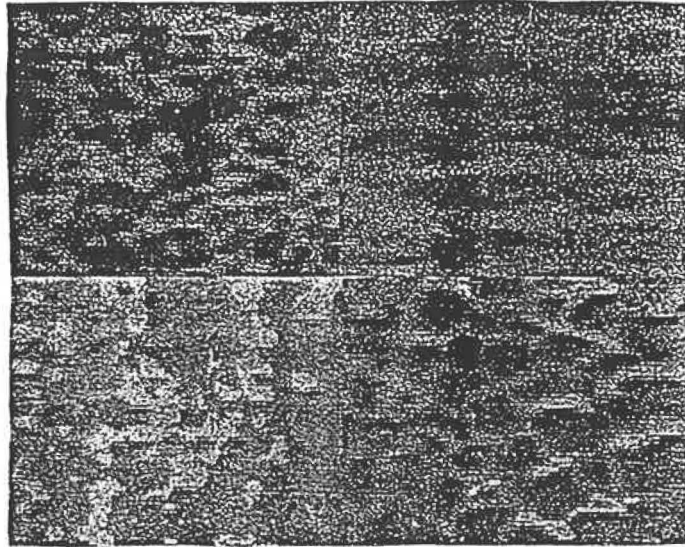


Figure 7.6 Composite texture polymer image (128 × 128)

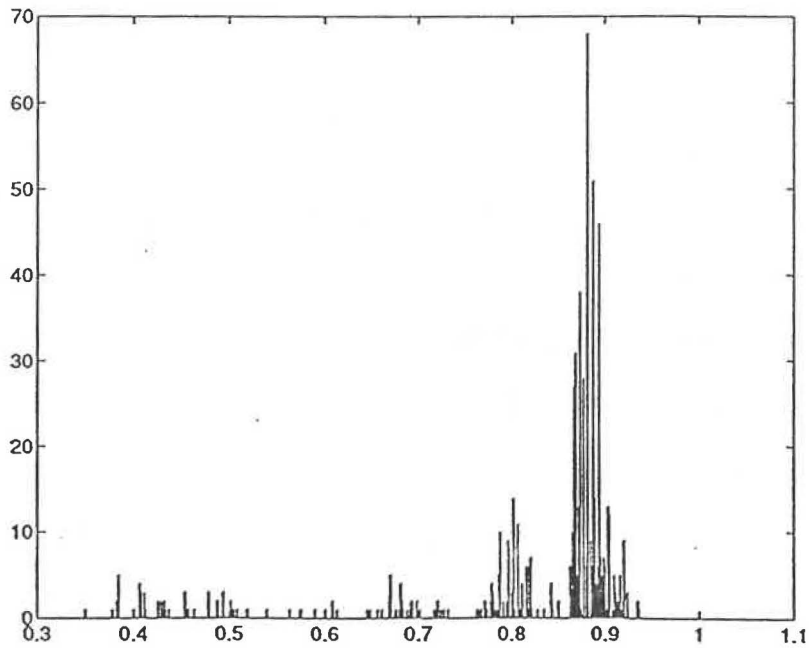


Figure 7.7 Histogram of fractal dimensions for the composite texture image

separated fractal dimensions. The histogram for the whole image is shown in Figure 7.7 and the segmentation was done interactively to give the best results. Figure 7.8 shows the result of the segmentation. Comparing with the original image, we can see that most of the misclassifications occur at the edges.

Another composite image (Figure 7.9) formed by four textures from the Brodatz album is used for testing the segmentation results with and without the presence of noise. The textures used are cotton canvas, burlap, raffia looped to a high pile and expanded mica in that order. It should be noted that no care was taken in arranging the texture to avoid misclassifications. Figure 7.10 shows the 3-D plot of the fractal dimensions for the composite image. The histogram of the fractal dimensions for the composite is shown in Figure 7.11 and the results of segmentation shown in Figure 7.12. The results for 1-D data shows that the estimators tend to under estimate the value of the fractal dimensions as  $H$  approaches 1 and degraded performance is obtained in the presence of noise. Even though expanded mica has this property, the segmentation achieved is good.

The image was then corrupted by adding Gaussian noise with S/N 30db. Figure 7.13 shows the histogram of fractal dimensions for this image and it can be noticed that some of the higher values of fractal dimensions have been under estimated. The segmentation result is shown in Figure 7.14 and the performance is acceptable. The comparatively poorer performance in the expanded mica section can be attributed to the fact that the (approximation to) FBM graph is very smooth in this case and the noise adds fragmentation to the curve. Figures 7.15 and 7.16 show the result of segmentation of the composite and the noisy composite image as 3-D plots.

It can be concluded that the fractal model is a powerful mechanism to describe textures and the application of the fractal dimension feature if coupled with even a simple additional feature like variance would yield excellent results. It may be

successful even in cases where the textures have the same fractal dimensions but different lacunarities.

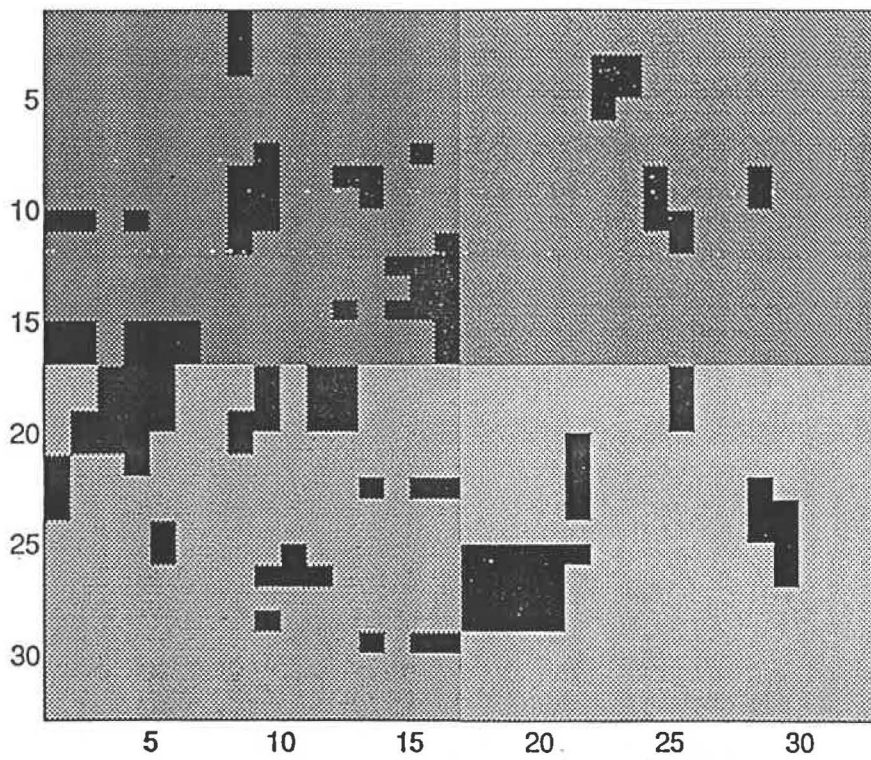


Figure 7.8 Result of segmentation of the composite polymer image

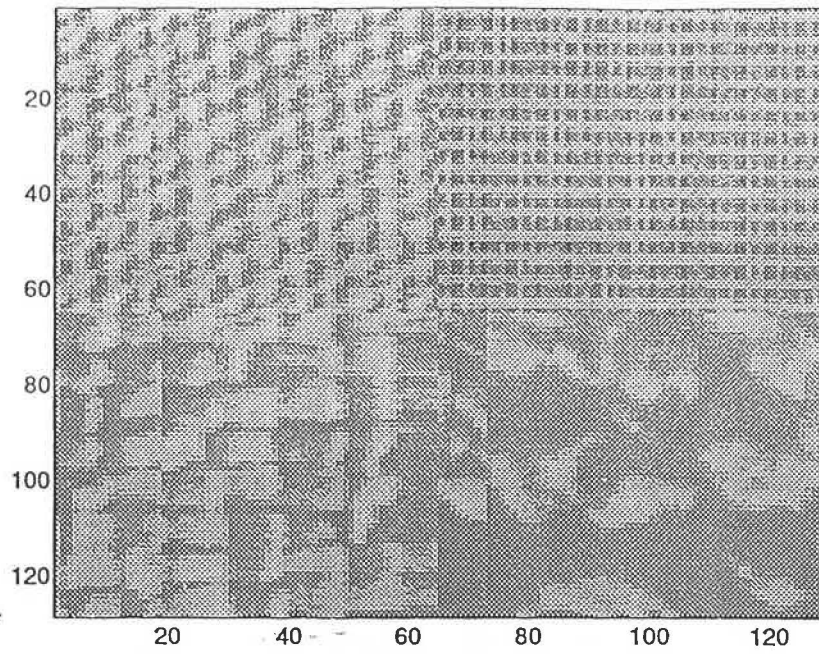


Figure 7.9 Composite Brodatz texture image

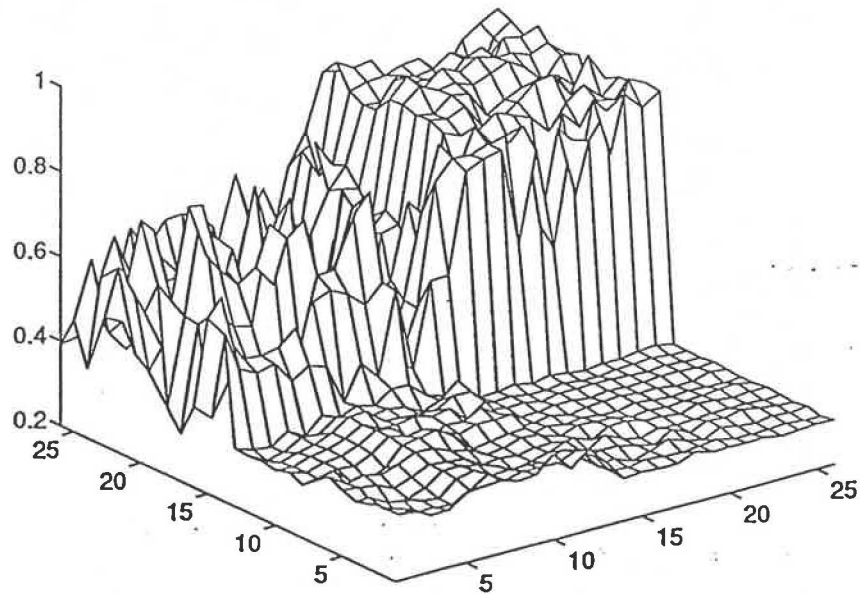


Figure 7.10 3-D plot of the fractal dimensions for the composite image

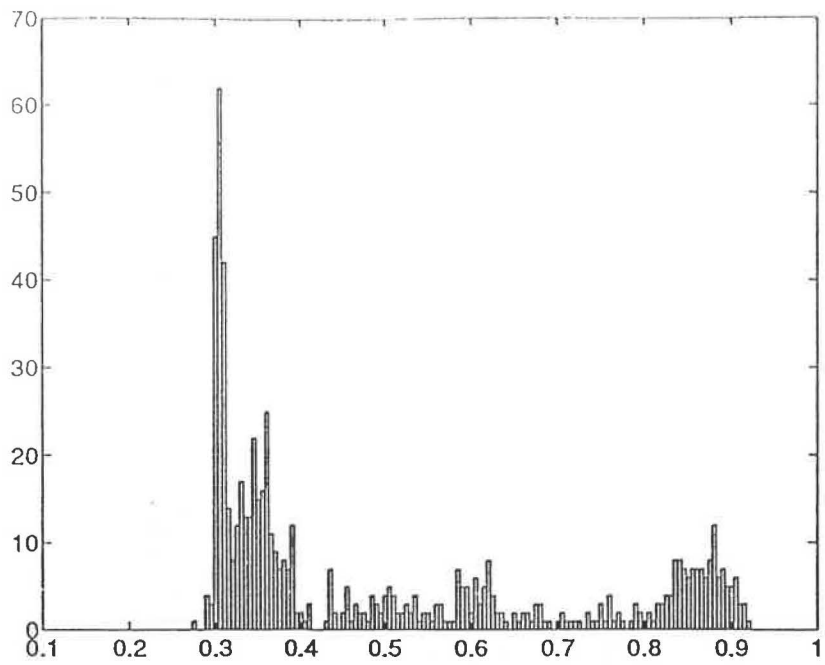


Figure 7.11 Histogram of fractal dimensions for the composite Brodatz texture

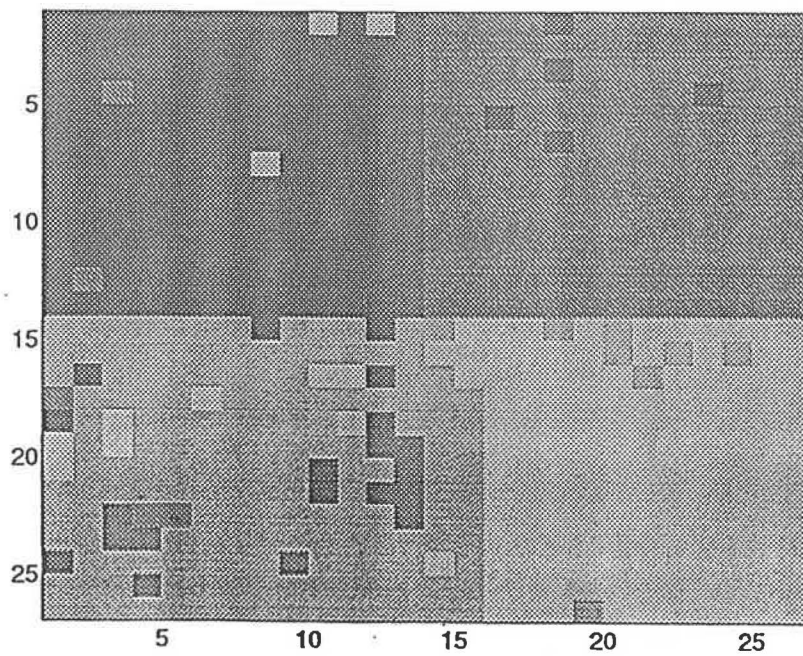


Figure 7.12 Results of segmentation of the Brodatz image

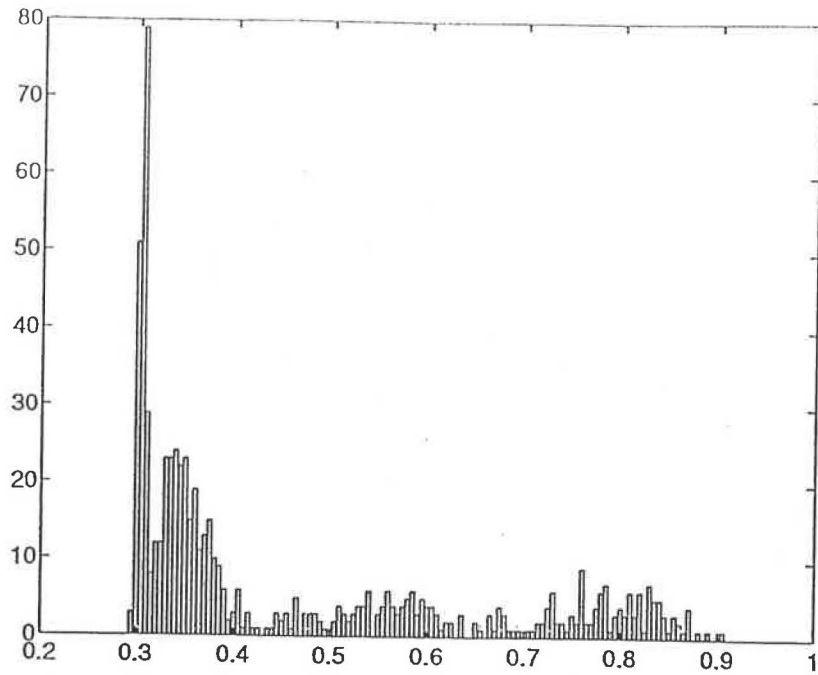


Figure 7.13 Histogram of fractal dimensions for the noisy Brodatz texture

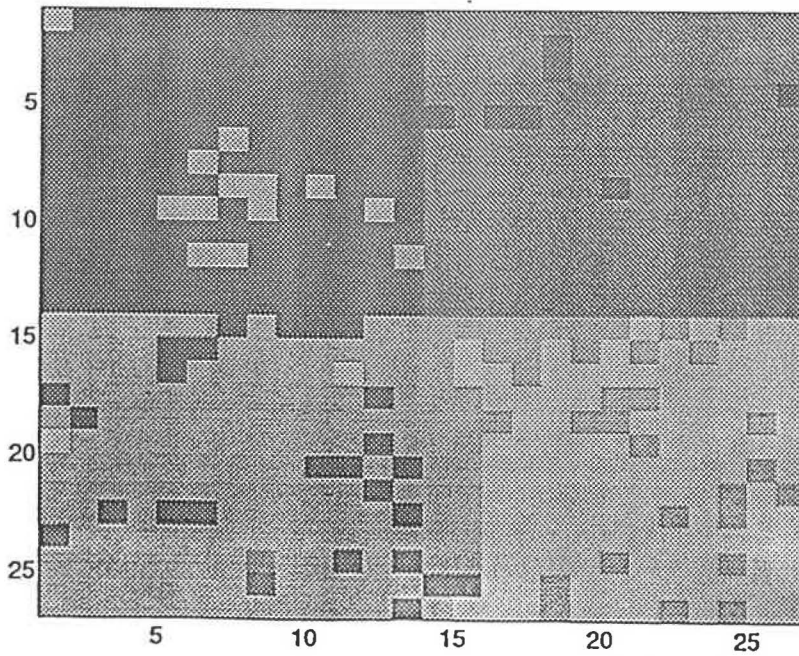


Figure 7.14 Result of segmentation of the noisy Brodatz composite image

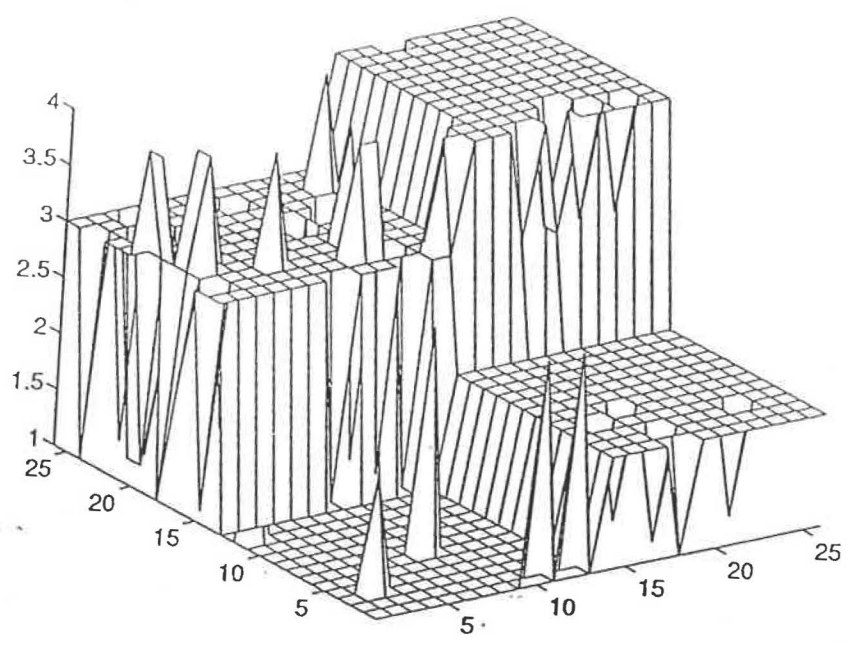


Figure 7.15 Result of segmentation of composite image shown as a 3-D plot

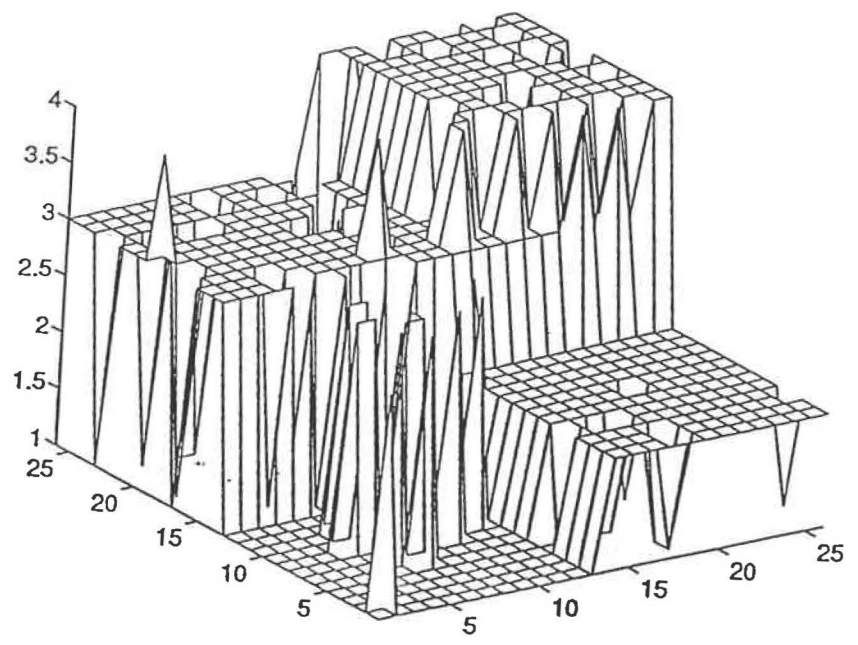


Figure 7.16 Result of segmentation of noisy image shown as a 3-D plot

## CHAPTER 8

### CONCLUSIONS AND FUTURE WORK

The robustness of the MLE estimator has been shown on different 1-D data sets and has been compared with the RD and the PSD methods. Characterization of a single texture image and segmentation of a composite texture image has been achieved using line to line formulation yielding good results even when the processes are unsupervised. It can be concluded that fractal modeling is a powerful tool in texture analysis. If it is used in conjunction with another appropriate texture feature (second moment for example) it has the potential to become a very powerful method in image processing/machine vision applications.

The degradation of the MLE performance in the presence of high noise power even when knowledge of the noise process is assumed has to be investigated. The estimation performance in the presence of multiplicative noise has to be investigated also. The performance of the estimation using the wavelet transform should be compared with this method. The estimation process should also be made faster for real time applications like automatic semiconductor wafer inspection.

## REFERENCES

1. B.B.Mandelbrot, The Fractal Geometry of Nature, New York: Freeman, 1982.
2. B.B.Mandelbrot, J.W.Van Ness, "Fractional Brownian Motions, Fractional Noises and Applications," SIAM Rev 10:422-437, 1968.
3. B.B.Mandelbrot, "Stochastic models for the Earth's relief, the shape and the fractal dimension of the coastlines and the number area rule for islands," Proc. Nat. Acad. Sci., Vol. 72, No. 10:3825-3828, Oct. 1975.
4. B.B.Mandelbrot, "Self-affine Fractals and Fractal Dimension," Physica Scripta, 32:257-260, 1985.
5. S.Chesters, H.C.Wang, G.Kasper, "A Fractal based method for describing Surface Texture," Solid State Technology:73-77, January 1991.
6. P.Pfeifer, D.Avinir, A.Farin, "Ideally irregular surfaces of dimension greater than two in theory and practice," Surface Sci., Vol. 126:569-572, 1983.
7. A.L.Goldberger, D.R.Rignas, B.J.West, "Chaos and Fractal in Human Physiology," Sci. Am. ,262:42-49, 1990.
8. A.E.Jacquin, "Image Coding Based on a Fractal Theory of Iterated Contractive Image Transformations," IEEE Trans. Image Proc. , Vol. 1, No. 1:18-30, January 1992.
9. J.L.Vehel, "Fractal Probability Functions. An Application to Image Analysis," Proc. IEEE Computer Society Conf. on Comput. Vision and Pattern Recog. (CVPR) : 378-383, 1991.
10. P.Maragos, "Fractal Aspects of Speech Signals: Dimension and Interpolation," Proc. IEEE Intl. Conf. Acc. Speech and Signal Proc. :417-420, 1991.
11. P.T.Nguyen, J.Quinqueton, "Space filling curves and Texture Analysis," Proceedings of the 6 Intl. Conf. Pattern Recog. , Munich, Germany:282-285, 1982.
12. E.E.Peters, Chaos and Order in the Capital Markets, New York: John Wiley and Sons, 1991.
13. T.Lundahl, W.J.Ohley, W.S.Kuklinski, D.O.Williams, H.Gewirtz A.S.Most, "Analysis and Interpolation of Angiographic Images by use of Fractals," IEEE Comput. Cardiol., 1985.
14. A.P.Pentland, "Fractal-Based Description of Natural Scenes," IEEE PAMI, No. 6:661-674, Nov. 1984.

15. A.P.Pentland, "Shading into Texture," *Artificial Intelligence*, 29:147-170, 1986.
16. A.P.Pentland, "Fractal based Description," *Proc. Eighth Intl. Conf. Artif. Intell. , Karlsruhe (FRG) :973-981, 1981.*
17. P.Kube, A.P.Pentland, "On the Imaging of Fractal Surfaces," *IEEE Trans. Pattern Anal. Mach. Intell. PAMI 10:704-707, September 1988.*
18. H.O.Peitgen, D.Saupe (Eds.), *The Science of fractal Images*, New York: Springer-Verlag, 1988.
19. J.Feder, *Fractals*, New York: Plenum Press, 1988.
20. H.E.Schepers, J.H.G.M.Van Beek, J.B.Bassingthwaighte, "Four methods to estimate the fractal dimension from self-affine signals," *IEEE Eng. in Med. and Biol. :57-64, June 1992.*
21. Y.Ogata, K.Katsura, "Maximum Likelihood Estimates of the Fractal Dimension for Random Spatial Patterns," *Biometrika*, 78, 3:463-474, 1991.
22. J.M.Keller, R.M.Crownover, R.Y.Chen, "Characteristics of Natural Scenes Related to the Fractal Dimension," *IEEE Trans. Patt. Anal. Mach. Intell. , PAMI-9, No. 5:621-627, 1987.*
23. P.Flandrin, "On the Spectrum of Fractional Brownian Motions," *IEEE Trans. Info. Theory. , Vol. 35, No. 1:197-199, January 1989.*
24. P.Maragos, F.K.Sun, "Measuring the Fractal Dimension of Signals:Morphological Covers and Iterative Optimization," *IEEE Trans. on Sig. Proc. , Vol. 41, No. 1, January 1988.*
25. G.W.Wornell, A.V.Oppenheim, "Estimation of Fractal Signals from Noisy Measurements using Wavelets," *IEEE Trans. on Sig. Proc. , Vol. 40, No. 3:611-623, March 1992.*
26. T.Higuchi, "Relationship between the fractal dimension and the power law index for a time series:a numerical investigation," *Physica D*, 46:254-264, 1990.
27. B.B.Mandelbrot, "A fast fractional gaussian noise generator," *Water Resources Research*, Vol. 7, No. 3:543-553, June 1971.
28. J.B.Bassingthwaighte, R.B.King, S.A.Roger, "Fractal Nature of Regional Myocardial Blood Flow Heterogeneity," *Circ. Res. , 65:578-590, 1989.*
29. W.J.Conover, *Practical Non-Parametric Statistics*, New York: John Wiley and Sons, 1980.
30. R.Deutsch, *Estimation Theory*, Englewood Cliffs, N.J: Prentice Hall Inc. , 1965.

31. J.P.Box , G.M.Jenkins, Time Series Analysis, San Francisco, CA :Holden-Day, 1976.
32. G.M.Jenkins, D.G.Watts, Spectral Analysis and its Applications, San Francisco, CA: Holden Day, 1968.
33. A.Papoulis, Probability, Random Variables and Stochastic Processes, New York: McGraw Hill Inc. , 1991.
34. M.V.Berry, Z.V.Lewis, "On the Weierstrass-Mandelbrot Fractal Function," Proc. R. Soc. Lond. A370:459-484, 1980.
35. W.H.Press, S.A.Teukolsky, W.T.Vetterling, B.P.Flannery, Numerical Recipes in C, New York: Cambridge University Press, 1992.
36. H.W.Lilliefors, "On the Kolmogorov-Smirnov test for normality with mean and variance unknown," Journal of the American Statistical Association, 62:399-402, 1967.
37. M.A.Stephens, V.R.Maag, "Further percentage points for  $w_N^2$ ," Biometrika, 55:428-430, 1968.
38. T.Lundahl, W.J.Ohley, S.M.Kay, R.Siffert, "Fractional Brownian Motion:A Maximum Likelihood Estimator and Its Application to Image Texture," IEEE Trans. Med. Imag. MI-5:152-161, 1986.
39. A.H.Tewfik, Mohamed Deriche, "Maximum Likelihood Estimation of the Fractal Dimensions of Stochastic Fractals and Cramer-Rao Bounds," Proceedings of the IEEE Conf. on Acc. Speech and Sig. Proc. (ICASSP), pp. 3381-3384, July 1991.
40. R.M.Haralick, "Statistical and Structural Approaches to Texture," Proc. IEEE 67:786-804, 1979.
41. S.Peleg, J.Naor, R.Hartley, D.Avnir, "Multiple Resolution Texture Analysis and Classification," IEEE Trans. Patt. Anal. Mach. Intell. , No. 4:518-523, July 1984.
42. G.Medioni, Y.Yasumoto, "A note on using the fractal dimension for segmentation," IEEE Computer Vision Workshop, Annapolis, MD, 1984.
43. B.Schachter, N.Ahuja, "Random Pattern Generation Processes," Comp. Graphics and Image Processing, No. 10, 1979.
44. G.R.Cross, A.K.Jain, "Markov Random Field Texture Models," IEEE Trans. Patt. Anal. Mach. Intell. , PAMI Vol. 5, No. 1, January 1983.
45. N.Ahuja, A.Rosenfield, "Mosaic models for textures," IEEE Trans. Patt. Anal. Mach. Intell. , PAMI Vol. 3, No. 1, January 1981.

46. B.J.Super, A.C.Bovik, "Localized Measurement of Image Fractal Dimension using Gabor Filters," *Journal of Visual Communication and Image Representation*, Vol. 2, No. 2:114-128, June 1991.
47. J.Keller, S.Chen, R.Crownover, "Texture Description and Segmentation through Fractal Geometry," *Comput. Vision Graphics Image Process.* , 45:150-166, 1989.
48. T.J.Dennis, N.G.Dessipris, "Fractal modeling in image texture analysis," *IEE Proc.* , Vol. 136, Pt. F, No. 5:227-236, October 1989.
49. A.R.Rao, A Taxonomy for Texture Description and Identification, New York: Springer-Verlag, 1990.
50. A.R.Rao, R.Jain, "A Classification Scheme for Visual Defects Arising in Semiconductor Wafer Inspection," *Journal of Crystal Growth*, 103:398-406, 1990.
51. K.Falconer, Fractal Geometry:Mathematical Foundations and Applications, New York: Wiley, 1990.
52. A.Fournier, D.Fussel, L.Carpenter, "Computer rendering of stochastic models," *Commn. of ACM*, 25:371-384, 1982.
53. M.G.Petrolekas, Masters thesis, Dept. of Electrical Engg., Texas Tech University, 1991.
54. I.M.Young, J.W.Crawford, "The Analysis of Fracture profiles of Soil using Fractal Geometry," *Austr. Journal of Soil Res.*, Vol. 30, No. 3:291, 1992.
55. D.Thiebaut, "On the Fractal Dimension of Computer Programs and its Application to the Prediction of the Cache Hit-Miss Ratio," *IEEE Trans. on Comp.*, Vol. 38, No. 7:1012, July 1989.
56. J.M.H. Du Buf, "Abstract processes in texture discrimination," *Spatial Vision*, Vol. 6, No. 3:221-242, 1992.
57. N.Sarkar, B.B.Chaudhuri, "An efficient approach to estimate fractal dimension of textural images," *Pattern Recognition*, Vol. 25, No. 9:1035-1041, 1992.
58. P. Brodatz, Texture: A Photographic Album for Artists and Designers, New York: Dover, 1966.

APPENDIX A : CRAMER-VON MISES TEST

Table A.1 Lower tail percentage points for  $w_N^2$  for the Cramer-Von Mises test

N	0.005	0.01	0.25	0.05	0.10
2	0.0426	0.0433	0.0457	0.0496	0.0576
3	0.0312	0.0332	0.0377	0.0436	0.0529
4	0.0273	0.0300	0.0354	.0415	0.0509
5	0.0258	0.0287	0.0342	0.041	0.051
8	0.025	0.027	0.033	0.039	0.048
10	0.024	0.027	0.032	0.038	0.047
20	0.022	0.025	0.031	0.037	0.047
$\infty$	$\infty$	0.025	-	0.037	0.046

Table A. 2 Upper tail percentage points for  $w_N^2$  for the Cramer-Von Mises test

N	$\alpha$	0.05	0.025	0.01	0.005
2	0.10	0.424	0.490	0.550	0.583
3	0.343	0.423	0.509	0.622	0.707
4	0.337	0.435	0.529	0.653	0.747
5	0.341	0.441	0.540	0.671	0.771
8	0.343	0.451	0.556	0.698	0.806
10	0.346	0.454	0.562	0.707	0.818
20	0.347	0.459	0.572	0.724	0.841
$\infty$	0.349	0.461	0.581	0.743	0.870
	0.347				

APPENDIX B

LILLIEFORS TEST

Table B. 1 Level of Significance for D for Lilliefors test  
 $D = \text{Max} | F^*(X) - S_N(X) |$

Sample Size N	0.2	0.15	0.1	0.05	0.01
4	0.300	0.319	0.352	0.381	0.417
5	0.285	0.299	0.315	0.337	0.405
6	0.265	0.277	0.294	0.319	0.364
7	0.247	0.258	0.276	0.300	0.348
8	0.233	0.244	0.261	0.285	0.331
9	0.223	0.233	0.249	0.271	0.311
10	0.215	0.224	0.239	0.258	0.294
11	0.206	0.217	0.230	0.249	0.284
12	0.199	0.212	0.223	0.242	0.275
13	0.190	0.202	0.214	0.234	0.268
14	0.183	0.194	0.207	0.227	0.261
15	0.177	0.187	0.201	0.220	0.257
16	0.173	0.182	0.195	0.213	0.250
17	0.169	0.177	0.189	0.206	0.245
18	0.166	0.173	0.184	0.200	0.239
19	0.163	0.169	0.179	0.195	0.235
20	0.160	0.166	0.174	0.190	0.231
25	0.149	0.153	0.165	0.180	0.203
30	0.131	0.136	0.144	0.161	0.187
Over 30	0.736/ $\sqrt{N}$	0.768/ $\sqrt{N}$	0.805/ $\sqrt{N}$	0.886/ $\sqrt{N}$	1.031/ $\sqrt{N}$